Observing atmospheric convection with dual-scanning lidars

Christiane Duscha[1], Juraj Pálenik[2], Thomas Spengler[3], and Joachim Reuder[1]

[1]Geophysical Institute, and Bergen Offshore Wind Centre, University of Bergen, and Bjerknes Centre for Climate Research, Bergen, Norway
[2]Department of Informatics and Geophysical Institute, University of Bergen, Bergen, Norway
[3]Geophysical Institute, University of Bergen, and Bjerknes Centre for Climate Research, Bergen, Norway

Correspondence: Joachim Reuder (joachim.reuder@uib.no)

Abstract. While convection is a key process in the development of the atmospheric boundary layer, conventional meteorological measurement approaches fall short in capturing the evolution of the complex dynamics of convection. To obtain deeper observational insight into convection, we assess the potential of a novel dual-lidar approach. We present the capability of two pre-processing procedures, an advanced clustering filter instead of a simple threshold filter, as well as a temporal interpolation,

5 to increase data availability and reduce errors in the individual lidar observations that would amplify in the dual-lidar retrieval. To evaluate the optimal balance between spatial and temporal resolution to sufficiently resolve convective properties, we test a set of scan configurations. We tested the dual-lidar setup at two Norwegian airfields in a different geographic setting. We present a retrieval of the convective flow field in a vertical plane above the airfield for each of these setups. Both pre-processing procedures show an improving effect on the data availability and quality and are applied to the observations used in the dual-lidar

10 retrieval. All tested angular resolutions captured the relevant spatial features of the convective flow field and balance between resolutions can be shifted towards a higher temporal resolution. Based on the evaluated cases, we show that the dual-lidar approach sufficiently resolves and provides valuable insight into the dynamic properties of atmospheric convection.

1 Introduction

Convection plays a key role in the redistribution of energy, heat, moisture, momentum, and matter in the atmospheric boundary

15 layer. Convection also contributes to the deepening of the boundary layer, the formation of convective clouds, and the generation of precipitation (Stull, 1988; Emanuel et al., 1994). Accurately resolving or parameterizing convection in our weather and climate models is thus of great importance. However, the adequate physical and dynamical representation of atmospheric convection in our models remains challenging (Siebesma et al., 2007; Prein et al., 2017). Given the complex three-dimensional and short-lived nature of convection, conventional meteorological instrumentation is often unsuitable (Kunkel et al., 1977; Geerts

20 et al., 2018) and we have to resort to Large-Eddy Simulations (LES) to constrain and validate parametrizations (Brown et al., 2002; Siebesma et al., 2007). Hence, there is a demand for high-resolution and long-term observations of the multi-dimensional character of convection to reveal its structural evolution. Here, we propose and assess a setup for such observations based on dual-scanning lidars.

Early, aerosol-backscatter lidar observations have demonstrated the potential of scanning lidars to capture the size and
25   life-cycle of convective thermals in the boundary layer (Kunkel et al., 1977). Lidar technology has advanced significantly since
then with substantially increased spatial and temporal resolution. In addition to aerosol and cloud-particle backscatter, Doppler
lidar can also obtain the the wind velocity field projected onto the lidar's beam. Lidar scan configurations and setups have been
developed and optimized to retrieve wind vector profiles (e.g Werner, 2005; Calhoun et al., 2006), or even in multi-dimensional
space when combining multiple instruments (e.g Newsom et al., 2005, 2008; Iwai et al., 2008; Stawiarski et al., 2013; Adler
30   et al., 2020; Haid et al., 2020).

Single profiling lidars are able to capture properties of convective structures that move over the instrument within time scales
that are shorter than the lifecycle of the convective structures (Duscha et al., 2022). However, these structures were mainly
found in the marine boundary layer under extreme atmospheric conditions in the presence of strong advection. Over land,
however, convection is often more localized and the time scale of horizontal displacements by advection are usually slower than
35   the lifecycle of the convective structures (Kunkel et al., 1977). Hence, a more advanced approach is required to sample these
land-based convective structures. We propose and evaluate the potential of a dual-lidar setup that obtains the convective flow
field in a vertical two-dimensional cross-section.

There have been attempts to characterize convection with such dual-Doppler lidar setups. Röhner and Träumner (2013)
evaluated variance profiles of convection with a dual-lidar setup in a vertical plane. However, they only utilize certain points
40   along two lines within this cross-section and thus do not make use of the entire plane. Iwai et al. (2008) present a retrieval
of all three wind components of the convective flow field on a three-dimensional cartesian grid, using a set of overlapping
near-horizontal planes of two scanning lidars and assuming continuity to retrieve the vertical wind component. The time scale to
obtain one retrieval based on a full set of scans, however, exceeds the typically expected lifecycle of the convective structures of
interest and thereby limiting its assessment.

45   Motivated by the shortcomings of earlier attempts, we develop and optimize a methodology for the use of dual-scanning
Doppler lidars to probe the atmospheric convection in a vertical cross-section. We evaluate the benefit of improved filtering
and temporal interpolation of the lidar scans and investigate the optimal balance between temporal and angular resolution of
the scans. We present two cases, obtained during convective days at two small airports in Norway. Based on the retrieved flow
fields, we evaluate the setup's ability to capture the development of atmospheric convection, yielding representative convective
50   characteristics.

Evaluating the potential of the dual-lidar approach to accurately sample the convective flow is a part of gLidar (Pálenik, 2022).
The project aims to enhance sampling capacity and understanding of convection by combining Eulerian (lidar) and Lagragian
observations. The latter are based on voluntary observing pilots of sailplanes, hang gliders, and paragliders, equipped with
instrumentation to measure and log real-time position together with temperature, humidity, and pressure. These gliders utilize
55   convective updrafts to gain altitude and hence also provide vertical convective velocities as well as temperature and humidity
anomalies of the convective updraft. Environmental profiles outside the convective updrafts are obtained from parts of the flight
track outside convective plumes or from a skydiving airplane that is also equipped with the identical sensors. The collocation of

this in situ data together with the dual-lidar retrievals is utilized in the empirical convection model by Pálenik et al. (2020) to enhance our process understanding of convection in the atmospheric boundary layer.

60   Overall, our study proposes the dual-lidar setup as a novel observational tool to probe the convective flow field. A long-term installation of the setup could provide a sufficient observational basis to validate the representation of convection in LES or in parametrizations schemes of weather and climate models. Similar dual-lidar setups can be used to study the interaction of convection with obstacles, such as topography, larger constructions, and wind turbines. In combination with remote-access solution and processing capabilities, now-casting of current flow conditions, for example for take off and landing risk assessments

65   at airports, is feasible.

2   The experiment

2.1   The sites

We have chosen two small airports in Norway for sailplanes and small motorplanes as measurement sites for the dual-lidar experiment. From 12 May 2021 until 07 June 2021, we installed two Windcube-100S scanning lidars, an automatic weather

70   station (AWS), and a surface energy balance station (SEBS) at Vaksinen airport, Os, in Western Norway, ca. 25 km South of Bergen. The same instrumentation was deployed from 14 July 2022 until 30 July 2022 for the second field campaign at Starmoen airport, Elverum, in Eastern Norway, about 120 km Northeast of Oslo. Figure 1 shows the measurement sites and the location of the instrumentation and table 1 documents the coordinates of each instrument.

Table 1. Coordinates of the instrumentation at Vaksinen airport and Starmoen airport. The numbering of the lidars corresponds to the respective serial numbers of the WindCube-100S series.

	Coordinates (°N, °E)	
	Vaksinen	**Starmoen**
Lidar-34	Not installed	60.874353, 11.6793316
Lidar-37	60.1936435, 5.4242786	60.880778, 11.6703844
Lidar-40	60.1891728, 5.4166957	Not installed
AWS	60.1926322, 5.4216220	60.8787601, 11.6741224
SEBS	60.1925799, 5.4216013	60.8743419, 11.6794812

2.2   The instrumentation

75   The AWS provides background information on the basic meteorological parameters of pressure, temperature, humidity, wind speed, wind direction, incoming shortwave radiation, and precipitation in 1-min temporal resolution. The SEBS measures the four components of the radiation balance, i.e., incoming and outgoing short- and longwave radiation, together with highly resolved (20 Hz) measurements of temperature, humidity, and three dimensional wind speed, each variable at a single altitude
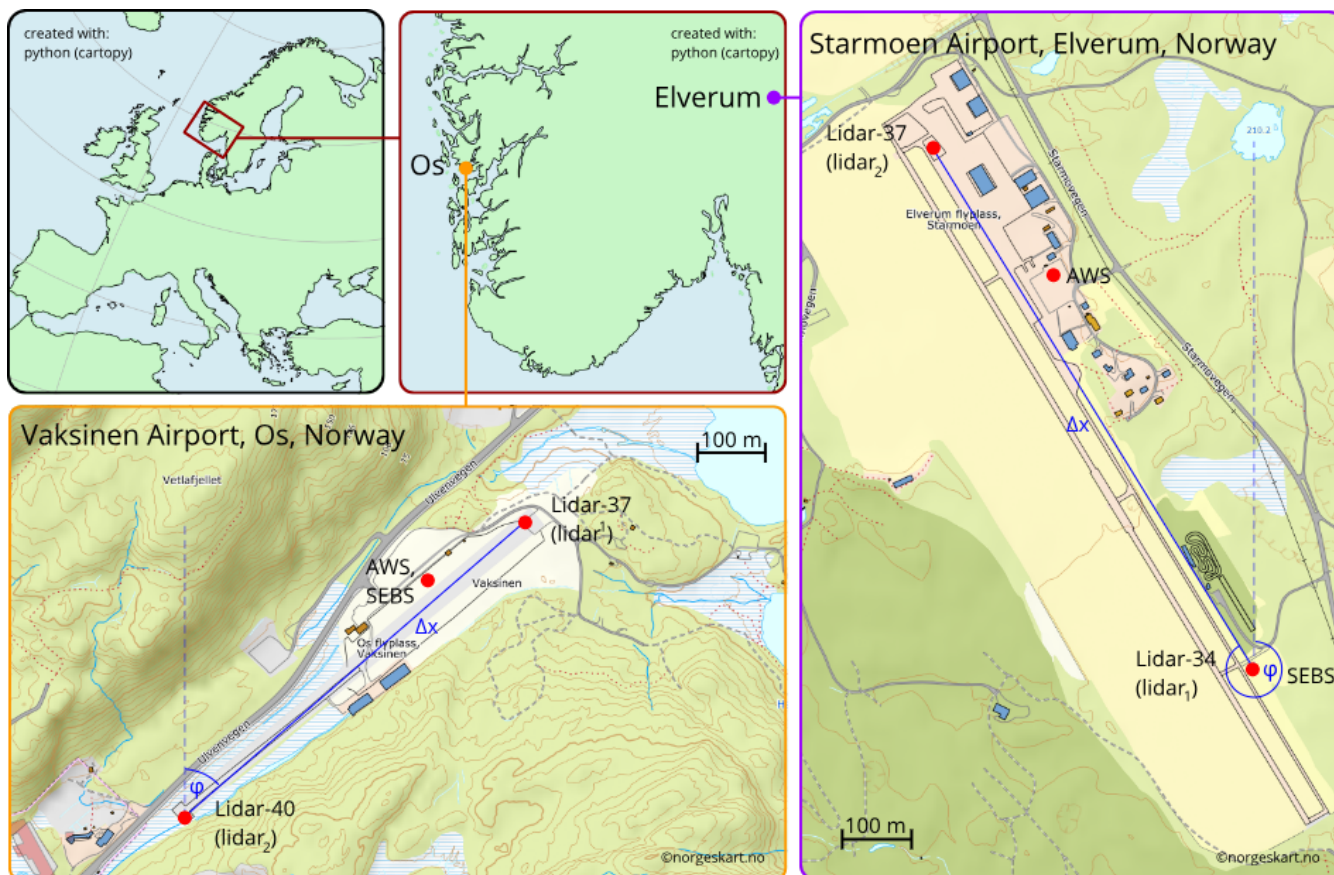
Figure 1. Location of the measurement sites and instrument setup. Top left: overview map of Europe. Top center: Zoom in to southern Norway with markers for the location of Os (orange) and Elverum (purple). Bottom left: Overview of the measurement site on Vaksinen airport in Os with locations of the utilized lidars, AWS, and SEBS indicated by red markers, and distance, Δx, and angle, φ, relative to north between the lidars indicated in blue. Right: Overview of the measurement site on Starmoen airport near Elverum with locations of the utilized lidars, AWS, and SEBS indicated by red markers, and Δx, and φ indicated in blue.

above ground. In addition the SEBS also provided profile measurements of temperature, humidity and wind at 1 m, 2 m and

80   4 m above the surface in a lower resolution (1 min). In this study, we utilize measurements from AWS and SEBS mainly to identify precipitation free periods that favour convective conditions throughout the two campaigns and to estimate the surface heat flux (see Sect. 5.2) and flux Richardson number (see Sect. 5.3) as indication for the presence of convection.

In both campaigns the two scanning lidars were installed with a relative distance, Δx (m), and angle, φ (°), relative to north to each other on opposing ends of the runway of the corresponding airfields (Figure 1). The lidars observe radial velocity,

85   v_r (m s^{-1}), which is the velocity of the wind projected to the line of sight (LOS) of the lidar beam. The scanning lidars, used in the experiment, can be programmed to point towards a direction corresponding to a certain azimuth angle, α (°), and an elevation angle, θ (°). For each combination of α and θ, v_r values are simultaneously obtained at several ranges, r (m), from the lidar.

Along the lidar beam, each v_r value is observed as a composite of the Doppler velocity of all particles, which contribute to lidar's back-scattering signal (e.g. Aerosols) within the lidar range gate length, Δr (m). The strength of the particle back-scatter is related to the signal to noise ratio, SNR (dB), which is also recorded by the lidar. By default, the distance between the range gates, which defines the range gate resolution, r_{res} (m), is equal to Δr. Yet, r_{res} can also be set manually, e.g. smaller than Δr, such that range gates overlap. The minimum range, r_{min} (m), needs to be at least $2 \cdot \Delta r$ and the maximum range, r_{max} (m), is dependent on the number of utilized range gates, N_{gates}, and r_{res}. Table 2 summarizes the lidar parameter specifications utilized during the two campaigns.

Table 2. Dual-lidar setup specifications for the two sites on Vaksinen airport and Starmoen airport.

	Vaksinen	**Starmoen**
Δx (m)	669	863
φ (°)	40	326
r_{min} (m)	50	50
r_{max} (m)	3000	3146
Δr (m)	25	25
N_{gates}	119	259
r_{res} (m)	25	12

2.3 The lidar strategy

We utilized two lidar measurement strategies. In both campaigns, we sampled the three-dimensional wind profile using a Doppler beam swinging mode (DBS) with five consecutive beams: four beams, which are of perpendicular or opposed $\alpha = (0°, 90°, 180°, 270°)$, each with $\theta = 75°$. The fifth beam points upward with $\theta = 90°$. The DBS is programmed to run for a duration, D_{run}, of 10 min within each hour. We retrieve an average of the wind profile over these 10 min, which we assume to be the representative profile for the corresponding hour.

The main strategy of the experiment aims to enable a retrieval of the plane-parallel horizontal, and the vertical velocity components, u and w (m s^{-1}), in a vertical cross-section above the runway of each airport. As displayed in Figure 2, this is achieved by range height indicator (RHI) scanning patterns performed by each lidar. Here, the lidar points horizontally to the complementing lidar (lidar$_1$: $\alpha = \varphi$, lidar$_2$: $\alpha = \varphi + 180°$, with $\theta = 0°$ orientation in direction of φ) and then performs a continuous scan by changing θ (lidar$_1$: from $\theta = 0°$ to $150°$, lidar$_2$: $\theta = 180°$ to $30°$). The accuracy of the horizontal (azimuth) alignment was assured by a hard-target calibration (Leosphere, 2022) of each lidar at the start of the campaigns. We utilize a retrieval to estimate u and w from overlapping RHI scans of the two lidars in the vertical cross-section above the runway. The retrieval combines v_r values of the two lidars with different polar coordinate systems and achieves u and w values on a cartesian grid (see Figure 2). We document further details of this retrieval method and its shortcomings in Sect. 4.

Convection is a dynamic process, which may rapidly modify u and w on short time scales and small spatial scales. It is therefore an important goal of this study to investigate the combination of temporal and spatial RHI scan resolution that
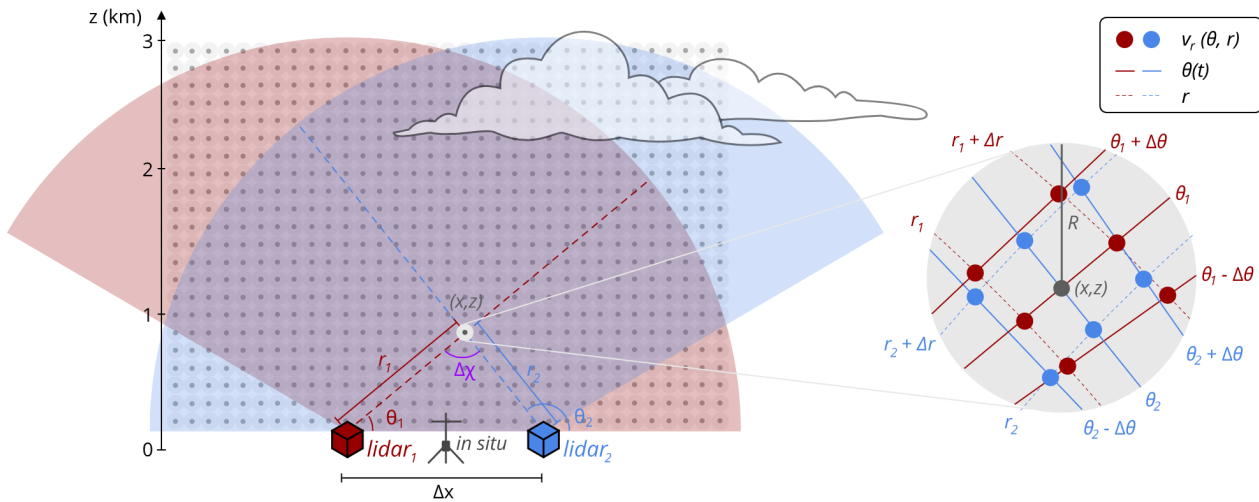
Figure 2. Vertical cross-section of the dual-lidar setup utilized during the campaigns at Vaksinen airport and Starmoen airport, respectively. The transparent red and blue surface areas represent the angular range covered by the RHI scans of the individual lidars, which are represented by the red and blue boxes. The dark grey dots represent a schematic of the cartesian retrieval grid. A zoom in on to the polar grid of the two lidars and the corresponding positions of all v_r values used for the retrieval of u and w in an exemplary point (x, z) of the cartesian grid is shown on the right hand side of the figure.

accurately captures the development of the convective circulation. The combination of the following parameters determines the temporal and spatial resolution of a single RHI scan. The scan speed, v_{scan} (° s^{-1}), determines the duration, D_{scan} (s), of a single RHI scan, which spans a certain range of θ (i.e. 150°; from $\theta = 30°$ to $\theta = 180°$). The product of v_{scan} and the integration
115   time, T_{int} (s), of the Doppler velocities that contribute to a single v_r values determines the angular resolution, $\Delta\theta$ (°), of the RHI scan.

High angular (spatial) resolution can be achieved with a low v_{scan} at the cost of a a long D_{scan} and hence a low temporal resolution when keeping angular range and T_{int} constant. On the other hand, by decreasing T_{int}, the angular resolution can be increased without changing v_{scan} and consequently without sacrificing temporal resolution for covering the same angular range
120   in a scan. However, short T_{int} can result in poor quality of the measured data due to low SNR.

During the two campaigns, we tested out different scanning configurations with varying balance between temporal and spatial resolutions, as well as integration time. These configurations are summarized in Table 3.

A major goal of the Vaksinen campaign was to evaluate the ability of different scan configurations to accurately map convection. At Vaksinen airport, several scanning patterns with either high temporal, or high spatial resolution, were run in
125   sequence within a one hour return period: First the wind profile was observed with a DBS scan for 10 min. Then the three scan configurations introduced in Table 3 were subsequently scheduled for 10 min each. This was followed by a series of fixed, out of

Table 3. Hourly returning schedule (*starting each hour at $\mathrm{hh:mm}$) of the RHI scan configurations during the Vaksinen and Starmoen campaign

Site	return *	D_{run} (min)	v_{scan} ($^\circ\,\mathrm{s}^{-1}$)	T_{int} (s)	$\Delta\theta$ ($^\circ$)	D_{scan} (s)
Vaksinen	10:00	10	1.0	0.5	0.5	150.0
	20:00	10	1.0	1.0	1.0	150.0
	30:00	10	4.0	0.5	2.0	37.5
Starmoen	00:00	50	2.0	0.5	1.0	80.0

plane RHI, and plan position indicator (PPI) scans for 20 min. These latter scan configurations of the experiment are, however, not relevant for this study and thus not further described.

At Starmoen airport, we aimed to study the evolution of convection more continuously than during the Vaksinen airport
130 campaign, utilizing longer D_{run} and sampling with only one scan configuration throughout the campaign (see Table 3). The RHI scan configuration is scheduled for 50 min, followed by a 10 min DBS scan. This schedule is repeated by each of the two lidars with a return period of 60 min throughout the campaign. The scan configuration chosen here is a compromise between the extremes of temporal or spatial resolution utilized during the Vaksinen campaign.

2.4 The challenges

135 During both campaigns, we met various challenges that affected the availability and quality of the data. On the Vaksinen airport site, there were several power outages that disordered the schedule of lidar-37 (north-eastern end of Vaksinen Airport, see Figure 1), demanding a manual fix on site. This led to a substantial loss of data during several convective days, as the failure was first detected after a site visit. Also, the data download from the internal computer of the lidars was very slow, which delayed full recovery of the data, processing, and the identification of further problems occurring during the campaign until after the recovery
140 of the instrumentation from the field. Despite the challenges encountered, we were able to secure representative observations from both lidars simultaneously during one very convective day (28 May 2021), which will be evaluated and discussed Sect. 6.

As a consequence of the challenges met during the Vaksinen airport campaign, we developed an upgraded version of our lidar setup. During the Starmoen campaign, the data was not only stored on the internal computer of the lidars, but also transferred via "sftp" protocol to a Raspberry Pi 4 Model B[1]. The Raspberry Pi was integrated into a remote access system developed by
145 the Geophysical Institute, University of Bergen, and solved the problem of the slow data download. The remote access system also includes an industrial router, which enabled real time data upload and visualization of the lidar observations on a server

---

[1]see https://www.raspberrypi.com

provided by the Norwegian Research and Education Cloud (NREC[2]), as well as a time synchronisation of the lidars independent
from GPS. This enabled us to identify and already fix problems occurring during the campaign and ensured that the schedule
of the lidar program was kept throughout the campaign. A future application of this remote access system is, among others, a

150   remote control and programming of the lidar in the field.

Nonetheless, the period of installation at Starmoen airport was impacted by several precipitation events during the first half
of the campaign, which almost completely depleted the aerosol content in the boundary layer. This strongly reduced the SNR
obtained by the lidars and hence the reliability of the observed v_r. It required several convective days after the precipitation
period for the SNR to increase such that a sufficient data availability of v_r for processing and data analysis was achieved. After

155   the precipitation period during the Starmoen campaign, mainly one convective day (29 July 2022) with weak synoptic wind and
strong fluxes qualified for further detailed analysis (see Sect. 6).

3   Processing of dual-scanning lidar observations

Before combining the v_r values from the two lidars into horizontal, retrieval-plane parallel (u) and vertical (w) wind components,
the RHI scan data from individual instruments requires processing. In particular, the data needs to be filtered for noise and

160   erroneous features. After filtering, we apply temporal gap filling using interpolation to achieve an increased temporal resolution,
instantaneous RHI scans, and replace discarded data points. These procedures and how they improve the reconstructed data are
described in the following sections.

3.1   Radial velocity filtering

In a first step, we remove all v_r observations with absolute values exceeding 30 m s^{-1}, as they are unrealistically high for

165   convective conditions. Further, we have observed three types of problems with the data: Individual data points with noise; larger
irregular "streak" patterns, which can be associated with range-folded ambiguities as described by Bonin and Brewer (2017); and
irregular patterns, which result from interaction with obstacles. We address these problems by using the Density-Based Spatial
Clustering of Applications with Noise (DBSCAN) algorithm, which was previously used by Alcayaga (2020) to filter PPI scans
of Doppler lidar observations. In contrast to conventional filters, this clustering algorithm does not apply a fixed threshold to

170   either SNR or v_r. Instead, the DBSCAN algorithm detects clusters of datapoints characterized by both v_r and SNR. Therefore,
it can distinguish between reasonable v_r observations and noise in the same SNR range. This allows for the recovery of reliable
v_r values for SNR values even below -30 dB, which would be lost if the SNR threshold of -27 dB that is suggested by the lidar
manufacturer (Leosphere) would be applied.

We use the implementation of the DBSCAN algorithm in the "scipy" python package (Virtanen et al., 2020) to identify

175   clusters of datapoints in the $\text{SNR} - v_r$ space. Figure 3 displays the application of the DBSCAN filter for one example RHI
scan obtained during the Starmoen campaign 29 July 2022, starting at 14:20 UTC. Here, v_r is scattered against SNR and data
points which are identified as reasonable by the DBSCAN filter are highlighted in blue, while data points identified as noise are

---

[2]see https://www.nrec.no
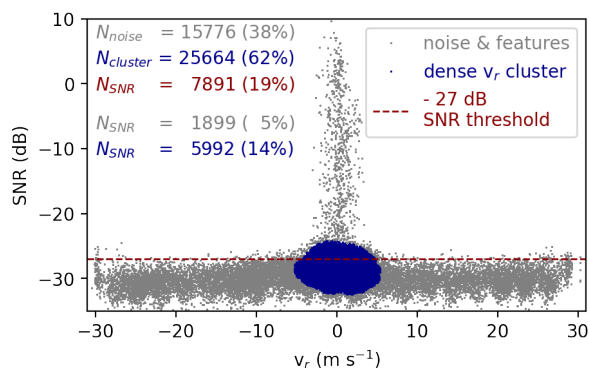
Figure 3. Scatter of v_r against SNR, with a DBSCAN identified cluster of dense scatterers (valid v_r) marked in blue and a rarefied scatterers (noise) marked in grey. The number of points (and the percentage relative to the whole data) which is classified as noise, N_{noise} (grey) and as cluster of reasonable points, $N_{cluster}$ (blue) are documented in the upper left corner. The dashed red line indicates the -27 dB SNR theshold. Values of v_r corresponding to SNR values below this line are discarded by the SNR filter. N_{SNR} (red) corresponds to the number of points (and percentage relative to the whole data) recovered by the SNR filter, while N_{SNR} (grey) and N_{SNR} (blue) correspond to the number of points (and percentage relative to the whole data) recovered by the SNR filter, yet attributed to the points corresponding to noise and reasonable values by the DBSCAN filter, respectively

displayed in grey. Specific to the number of points sampled in the RHI scan we apply a density radius $\epsilon = 0.6$ and a minimum number of samples $n_{sample} = 150$, which is dynamically adjusted depending on the sample size.

For the example displayed in Fig. 3, the DBSCAN algorithm identifies a cluster of reasonable v_r values, which makes up for 62% of the observed data points. The remaining 38% of the data points are classified as noise or features, such as range-folded ambiguities (Bonin and Brewer, 2017), obstacles, and clouds. The majority of noise is evident just below SNR = -27 dB, where v_r fluctuates between ± 30 m s^{-1}. In order to remove noise from the v_r data the conventional SNR threshold is therefore reasonably set to -27 dB. However, when applying the SNR threshold filter to the RHI scan, only 19% of the v_r values are kept and a large part of data identified as reasonable by the DBSCAN filter is discarded. Further, only 14% of the data points are both above the SNR threshold and within the DBSCAN cluster, while 5% of the data points which are above the SNR threshold, correspond to noise or irregular, erroneous features.

Figure 4 shows the RHI cross-sections of v_r and SNR values, that are scattered against each other in Figure 3, as well as the filtered v_r values using the SNR threshold and using the DBSCAN algorithm. The situation captured on the 29 July 2022 at Starmoen by this RHI scan is convective and rather complex, which is evident mainly from the convergence of the horizontal velocity close to the surface around the x = -1 km horizontal distance mark (Fig. 4a). The obtained SNR is very low (below -27 dB) both close to lidar and at a larger range (Fig. 4b). For r beyond ≈ 2 km distance from the lidar the v_r values are irregular and noisy, while they appear rather regular close to the lidar despite the comparable low SNR. Only for r between 0.8 km and 1.8 km from the lidar, the SNR is overall increased. Additionally, several features, which correspond to local, strongly increased SNR are visible (Fig. 4b). We observe range-folded ambiguities around $(x,z) = (1.0,0.5)$ km and $(x,z) = (-3.0,0.5)$ km,

a physical obstacle which blocks the LOS around (x,z) = (-1.2,0.0) km, and a cloud around (x,z) = (-2.0,2.3) km. These features are also apparent in the v_r values (Fig. 4a).
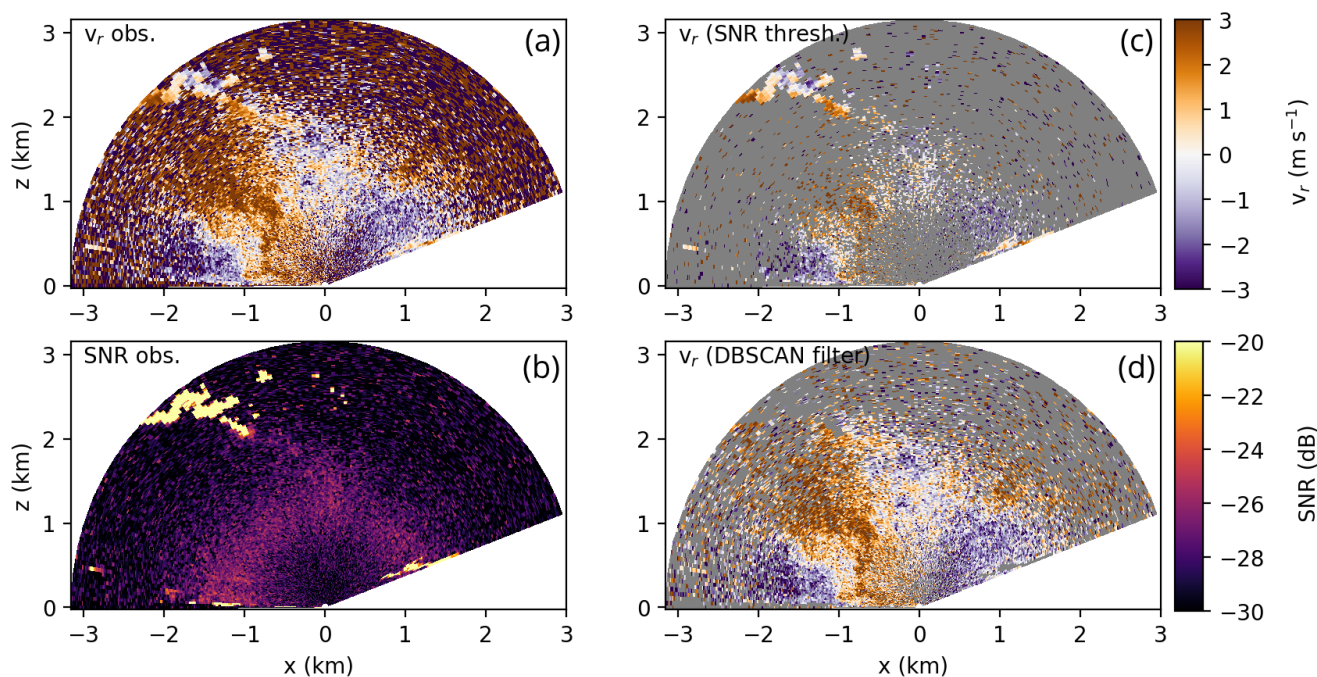
Figure 4. Sample RHI scan from the Starmoen campaign 29 July 2022 at 14:20 UTC with (a) observed v_r, (b) observed SNR, (c) filtered v_r using an SNR threshold, and (d) filtered v_r using the DBSCAN clustering algorithm. Grey areas correspond to values flagged as NaN by the (c) SNR threshold filter or (d) DBSCAN filter, respectively.

The SNR threshold filter (Fig. 4c) removes a large amount of v_r values within a 1 km radius around the lidar and at r larger than 2 km from the lidar. Yet, erroneous v_r values corresponding to range-folded ambiguities are not filtered out. On the basis of
200 the remaining v_r data, the convective circulation is hardly recognisable. The RHI scan, observed during the same time period from the complementary lidar experiences a similarly extreme reduction of v_r values when applying the SNR threshold filter (not shown here). As a consequence the region of valid overlapping v_r is even more reduced and will yield even a less valuable retrieval of u and w after applying the SNR threshold filter.

The DBSCAN filter, on the other hand, successfully removes noise, which is clearly evident at $r > 2$ km from the lidar
205 (Fig. 4d). Reasonable v_r values close to the lidar, but also at larger distances are not filtered out and the information about the convective flow field is retained. Further, most range-folded ambiguities and features caused by blocking of LOS by obstacles are removed from the data. Unfortunately, this also includes parts of the data points, obtained within clouds, which is of interest for the convective circulation.

The example presented in Figures 3 and 4 corresponds to conditions with comparably low aerosol content due to preceding
210   periods with precipitation during the Starmoen campaign. Considering the composite of relevant RHI scans throughout the
convective day at Starmoen (29 July 2022) which is presented in this study, the DBSCAN filter discards 61% of data points,
while the SNR filter discards 85% of data points. During the Vaksinen campaign, we did not sample any precipitation event
in the period prior to the convective day, which is presented as a show case in this study. As a consequence, aerosols could
accumulate in the boundary layer, and SNR was comparably high for the show case. Filtering by DBSCAN (38%) and SNR
215   threshold (60%) yielded comparably lower rates of removal for the evaluated convective day at Vaksinen (28 May 2021). Even
lower and more similar removal rates are found for the DBSCAN filter (19%) and the SNR threshold filter (23%) on 28 May
2021, when considering only the filtered values within the boundary layer (for boundary-layer depth estimation see Sect. 5.1).
Here, the DBSCAN filter outperforms the SNR threshold filter, mainly by removing noise and range-folded ambiguities which
are also present at SNR > -27 dB.

220   Due to the improved data quality and availability, we prepare the v_r data for further processing by applying the DBSCAN
filter to each RHI scan throughout the evaluated convective days of both campaigns. Since the DBSCAN algorithm is relatively
costly in terms of computational power, we store the filtered data in hourly netcdf files, along with the other relevant variables
observed by the lidar. This dataset is utilized in the following processing step.

3.2   Temporal interpolation

225   Dependent on the scan configuration (Tab. 3), each individual RHI scan takes a few tens of seconds up to 2.5 min. Consequently,
the RHI scans used for the reconstruction of the wind field between the two lidars are not instantaneous snapshots of the radial
velocity field. Only the observations along the beam of a single θ correspond to the same time step, within the same RHI scan.
Even if the RHI scans of the two lidars are perfectly synchronized, only a very small amount of spatially-overlapping points in
the cross-section (see i.e. Fig. 2 and Röhner and Träumner, 2013), are observed without any time lag between the two lidars. For
230   any fixed point in the overlap of the lidar scans, the maximum possible time difference between observations by each lidar is
bound by D_{scan}. If the time difference is considerably large, the convective wind field observed as v_r at a certain point in the
cross-section by one lidar can strongly differ from the wind field observed by the complementing lidar. Such temporal deviation
of the v_r observations in a given point propagates and amplifies as a temporal under-sampling error in the retrieval of u and w.
The consequences of such error for the retrieval is further specified in Sect. 4.2.

235   To reduce the impact of the temporally induced error, we test the usage of an instantaneous lidar cross-section, achieved
by temporal interpolation. For that, we interpolate linearly between each $v_r(r, \theta, t)$ and $v_r(r, \theta, t + D_{scan})$, located in the
same position in space (r, θ) yet at the time of the next scan $(t + D_{scan})$. The highest time resolution of the interpolated grid
corresponds to one RHI cross-section every T_{scan} of the respective scan configuration (see Table 3). From an interpolated array
of v_r values (with three dimensions: θ, r, t) we can now extract instantaneous cross-sections, where all v_r values correspond to
240   one specific time stamp. Only values corresponding to one single θ are actually observed by the lidar in this scan, the remaining
values are a result of the interpolation. A big advantage of the temporal interpolation is that we can utilize cross-sections from
the two lidars that correspond to the exact same t. Hence, when using temporal interpolation, not even a perfect synchronisation

of the RHI scans of the two lidars is required. The v_r values will still be most accurate around the θ that is observed at the time step the instantaneous scan is interpolated to. Synchronisation of the lidar scans mainly achieves that the line of no time lag is

245   located along the vertical profile above the mid point between the two lidars. Yet, convective eddies are not necessarily located directly in the middle of the lidars.

To demonstrate how the maximum possible error of the interpolated scan compares to the maximum possible error between non-interpolated, consecutive scans, we create an interpolated series. To achieve this, we interpolate between every second RHI scan obtained. Here, we actually create two interpolated series based both on the odd and the even RHI scans to double the

250   number of interpolated cross-sections. From both of these interpolated series we extract the v_r values, which correspond to $\theta(t)$ of the RHI scans, which are not used to create an interpolated series, respectively. Thus, we can estimate the average difference between an interpolated and the control RHI scan to quantify the error in the interpolated series, e_{int}. It should be mentioned that e_{int} is conservative, as the real interpolation is performed for only the half time step of the presented validation method. Also, in contrast to an instantaneous cross-section, here all extracted v_r values from the interpolated series correspond to the

255   maximum time lag, which is D_{scan}.

In a next step, we want to investigate the difference of e_{int} compared to the conservative temporal under-sampling error of the corresponding RHI scan series. We expect the maximum temporal under-sampling error for points where v_r values are measured with the maximum possible time lag of D_{scan} between the data points of two synchronized RHI scans. The average difference between two consecutive scans, therefore gives an estimate of the maximum expected temporal under-sampling error,

260   e_{con}, of the RHI scan series. In addition to e_{con}, we also estimate the temporal under-sampling error, merged for odd and evenly skipped RHI scan series, e_{skip}, which is the RHI scan resolution ($\sim 2 \cdot D_{scan}$) we used to estimate the interpolated series on which e_{int} is based on. Figure 5 shows time series of these three error estimates e_{skip}, e_{con} and e_{int}, how much e_{int} decreases in comparison to e_{con}, and how both of these error estimates behave in comparison to e_{skip} for two cases at the Starmoen and the Vaksinen site, respectively. We only consider values of the RHI scans, which are within the boundary layer, hence below the

265   boundary-layer depth, see. Sect. 5.1.

For the case on 28 May 2021 at the Vaksinen site (Fig. 5), the error estimates correspond to the scan configuration with the highest temporal scan resolution (D_{scan} = 37.5 s). Unfortunately, the two other scan configurations (see Table 3) utilized during the Vaksinen campaign do not provide a sufficient number of RHI scans to estimate a representative estimate of e_{int}.

With enhanced convective activity during the daytime hours, all three error estimates on 28 May 2021 (Fig. 5a) are generally

270   increasing from 07 UTC until 16 UTC. Within the early hours of the day (07 UTC – 09 UTC), the average total error between consecutive scans is low ($\sim 0.5 \mathrm{~m~s}^{-1}$) and increases to $\sim 1.5 \mathrm{~m~s}^{-1}$ at the peak of the convective activity (15 UTC – 16 UTC). Over the course of the day, e_{con} improves by 2 - 10% compared to e_{skip}, while e_{int} is consistently reduced by at least 10%, and up to 25% compared to e_{skip}. The improvement of e_{skip} is approximately $\sim$15% larger when using interpolation, instead of a doubled time resolution, almost throughout the whole convective day.

275   In comparison to the temporal error series displayed for the Vasksinen site (Fig 5a), each RHI scan utilized to estimate the temporal error at the Starmoen site (Fig 5b) takes approximately twice as long to complete (D_{scan} = 80 s). Overall, temporal under-sampling errors estimated for the connective day at Starmoen (Fig. 5b) are larger than at Vasksinen (Fig. 5a). Also, all
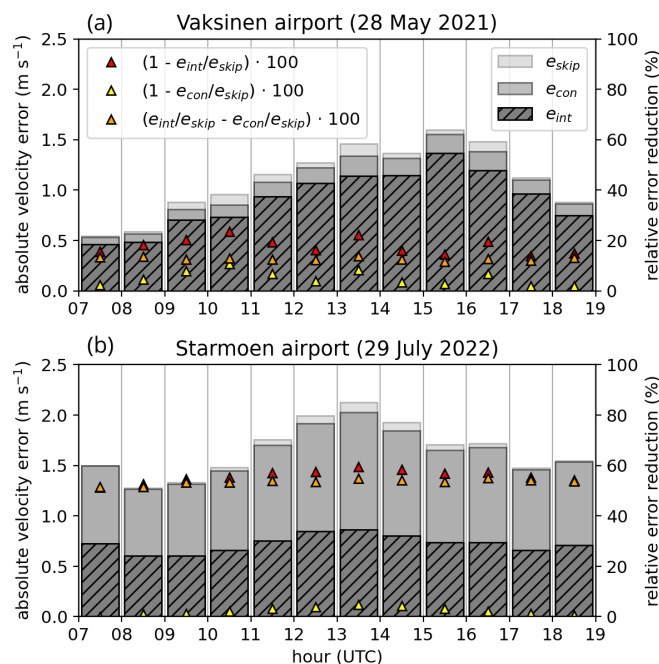
Figure 5. Maximum estimates of the temporal under-sampling errors for consecutive RHI scans (e_{con}) and for every second RHI scan (e_{skip}) as well as the temporal interpolation error (e_{int}) at (a) the Vaksinen site on 28 May 2021 between 07 UTC and 19 UTC and at (b) the Starmoen site on 29 July 2022 between 07 UTC and 19 UTC. For both sites, also the error reduction of e_{con} and e_{int} relative to the largest expected error e_{skip} is displayed with triangles on a secondary right-bound y-axis.

error estimates sampled on 29 July 2023 (Fig. 5b) reach their peak about two hours earlier (between 13 and 14 UTC), exceeding $2 \, \mathrm{m \, s^{-1}}$. Here, error reduction by simply doubling the temporal resolution of the RHI scans is negligible ($\leq 5\%$). Strikingly,

280 temporal interpolation strongly reduces the temporal under-sampling errors. For each displayed hour, e_{int} corresponds to less than half of the amount estimated for e_{skip} and e_{con}, respectively.

The much stronger error reduction by temporal interpolation for the Starmoen compared to the Vaksinen case can be partially linked to the longer ($D_{run} = 50 \, \mathrm{min}$) and hence more continuous RHI series at Starmoen. Potentially, also the representation of present, individual connective structure dynamics benefits stronger from temporal interpolation for the Starmoen than for

285 the Vaksinen case. Given that in both evaluated cases (Fig. 5a and b), the interpolation consistently reduces the temporal under-sampling errors, e_{skip} and e_{con}, as well as that it has a larger improving effect than simply increasing (here doubling) the time resolution, we utilize interpolated, instantaneous RHI scan series for all further processing steps.

4 Retrieval of the two dimensional wind field

In the next step, we combine the pre-processed (filtered and interpolated, see Sect. 3) v_r fields from both lidars to retrieve the u

290 and w fields for any point (x, z) in the lidar cross-section at discrete points in time. The temporal resolution of the retrieved cross-sections is the same as the temporal resolution of the utilized v_r fields. Since we save the v_r fields once per 1 s or even once per 0.5 s (see T_{int} in Table 3), we can retrieve u and w fields at any lower resolution that fits the purpose of the evaluated situation. The methodology to estimate u and w from independent v_r observations and the errors connected to the method are documented in the two subsections below.

295 4.1 Retrieval principle

At any position (x, z) within the vertical cross-section of the overlapping RHI scans, v_r is related to the instantaneous u and w components of the real wind projected to the θ-dependent LOS of the lidar beam,

$$v_r(x, z) = u(x, z) \cdot cos\theta + w(x, z) \cdot sin\theta \tag{1}$$

with (x, z) connected to θ and r by:

$$300 \quad \begin{pmatrix} x \\ z \end{pmatrix} = r \begin{pmatrix} cos\theta \\ sin\theta \end{pmatrix} + \begin{pmatrix} x_0 \\ z_0 \end{pmatrix} \tag{2}$$

where x_0 and z_0 define the relative position of the lidar to the origin point $(0, 0)$ of the cartesian coordinate system of choice for the retrieval. We set the location of the origin point at the individual ground level of the two sites in the middle of the two lidars, respectively.

To solve Equation 1 for u and w in the point (x, z), we need to construct an equation system utilizing at least two observations

305 of v_r, each obtained with an independent θ. Since lidars do not operate on a cartesian coordinate system (x, z), yet on individual polar coordinate systems (θ, r), there is very few combinations of θ and r of the two lidars, where the v_r observations fall into exactly the same point (x, z) in space (see Fig. 2). Still, retrieving the u and w on a cartesian instead of a polar retrieval grid is common approach to merge the observations of two lidars (e.g. Stawiarski et al., 2013; Adler et al., 2020; Haid et al., 2020).

Here, instead of using only two independent v_r observations in a single point (x, z), we construct an equation system (based

310 on Eq.1), containing all v_r values and their individual dependencies on r and θ, from the two lidars within a radius, R, around the cartesian point (x, z) of interest (see Fig. 2):

$$\begin{pmatrix} v_{r1}(r_1, \theta_1) \\ v_{r2}(r_2, \theta_2) \\ . \\ . \\ v_{rn}(r_n, \theta_n) \end{pmatrix} = \begin{pmatrix} cos\theta_1 & sin\theta_1 \\ cos\theta_2 & sin\theta_2 \\ . & . \\ . & . \\ cos\theta_n & sin\theta_n \end{pmatrix} \begin{pmatrix} u \\ w \end{pmatrix} \tag{3}$$

The equation system can also be written in vector and matrix format:

$$\boldsymbol{v_r} = \mathbf{N}\boldsymbol{v} \tag{4}$$

315 If more than two independent v_r observations are within R to construct the equation system, it is over-constrained. To solve the over-constrained equation system, which results from using R, we apply a least squares approach (see. Lai et al., 1978), using matrix inversion:

$$\hat{\boldsymbol{v}} = (\mathbf{N}^T\mathbf{N})^{-1}\mathbf{N}^T\boldsymbol{v_r} \tag{5}$$

where $\hat{\boldsymbol{v}}$ is the best fit of the u and w vector considering all utilized v_r observations.

320 It is also possible to incorporate v_r observations within a temporal radius, T_r, around the point of interest in time into the over-constrained equation system discussed above (see. Newsom et al., 2008). Yet, the usage of T_r rather represents a temporal average of the flow field and is not meaningful when using the instantaneous RHI scans, which result from the temporal interpolation (Sect. 3.2).

4.2 Retrieval errors and uncertainties

325 There are several sources of errors and uncertainties, which need to be considered for dual lidar retrievals. Many errors in the single lidar observation are projected and amplified in the co-planar retrieval, e.g. lidar specific uncorrelated noise and systematic error, and imprecise azimuth adjustment or levelling during the lidar setup and calibration (see e.g. Stawiarski et al., 2013).

  We attempt to minimize, or avoid the errors and error amplifications that are connected to the dual-lidar retrieval. One prominent error in the dual-lidar retrieval is the temporal under-sampling error, which is already mentioned in Sect. 3.2. The

330 observations of v_r of the two lidars may each correspond to a different state of u and w due to a time difference, at which v_r was observed by each lidar. Utilizing v_r values, which do not correspond to the same state of u and w in reality, will yield retrieved u and w values that may correspond to neither of the wind fields sampled by the individual lidar. The magnitude of the temporal under-sampling error is proportional to the absolute velocity difference in the flow field at the two time steps the two individual lidar obtained v_r (Stawiarski et al., 2013).

335 $\sigma_{time}(\Delta t) \approx |v_r1(t_1) - v_r2(t_2)|$ (6)

The time difference, $\Delta t = |t_2 - t_1|$, is dependent on the spatial location (x, z) in the dual lidar cross-section. To minimize the temporal under-sampling error, we use instantaneous RHI cross-sections, achieved from temporal interpolation instead of single scans (see Sect. 3.2). A further reduction of this error can be related to the usage of R and over-constrained equation systems to retrieve u and w for each point on the cartesian grid. Here, temporal errors, caused by small spatial displacement (within R)

340 between two scans are averaged out.

  For certain conditions the equation system (see Eq. 4) is ill-posed. In the case the angles θ_1 and θ_2 of the two intersecting lidars beams are both close to horizontal or close to vertical, the v_r observations are not really independent. This is the case for $\Delta\chi = |\theta_1 - \theta_2|$, which is either very small or very large (see Fig. 2). When the two lidars are both pointing horizontal, the horizontal component dominates the v_r observations of both lidars and the retrieval error of w is amplified. In this case $\Delta\chi$ is

345 either large (beams point towards each other), or small (both beam point in same direction horizontally). Mainly vertical pointing beams result in small $\Delta\chi$ and will amplify the retrieval error of u. Yet, with a sufficiently large Δx, which is the case for our

setups, the point, at which the retrieval error of u becomes important, is located above the retrieval grid. The amplification of the retrieval error, depending on $\Delta\chi$, is defined by the factor, σ_{amp} (see Stawiarski et al., 2013):

$$\sigma_{amp}^{i} = \sigma_{amp} \cdot \sigma^{i} = \frac{1}{sin^2(\Delta\chi)} \cdot \sigma^{i} \tag{7}$$

350   where σ^i is a placeholder for any single or dual lidar error (e.g. the temporal under-sampling error). We remove all retrieved values of w that correspond to $\Delta\chi > 150°$ and $\Delta\chi < 30°$, to avoid strongly amplified single and dual-lidar errors in the retrieval, such as those errors discussed in the paragraphs above.

Utilizing an over-constrained equation system enables to quantify the uncertainty in the retrieved wind field. The least-squares retrieval yields the best fit, hence a single retrieved value $\hat{u}$ or $\hat{w}$, respectively. By projecting these retrieved $\hat{u}$ and $\hat{w}$ values back

355   onto the LOS (see Eq. 1), which yield a single value $v_r(\hat{u}, \hat{w})$ for each grid point (x, z), we can estimate the root mean square error, $rmse$ (m s^{-1}):

$$rmse = \sqrt{\frac{1}{N} \sum_{n=1}^{N} |v_r(\theta_n, r_n) - v_r(\hat{u}, \hat{v})|^2} \tag{8}$$

The $rmse$ is estimated on basis of all N points of v_r within each R. This metric is useful to identify regions where processes are averaged over the area covered by R on the discrete cartesian retrieval grid, or where the temporal interpolation is not able to

360   accurately restore the dynamic behaviour of the convective circulation.

5   Convective boundary-layer parameters

In addition to the retrieval of the two dimensional velocity field $(\hat{u}, \hat{w})$, we estimate several boundary-layer parameters, based on complementing measurements from the lidars, the SEBS, and the AWS, but also from further processing the retrieved velocity field.

365   ### 5.1   Boundary-layer depth

We estimate the boundary-layer depth on the basis of the derivative of SNR with altitude. For both campaigns, the lidars are scheduled to obtain mainly RHI cross-sections. With Equation 2 we can estimate the z-coordinate corresponding to each SNR(θ, r) value and collapse all SNR values of a RHI cross-section to a single profile. We further average the profile for altitude bins of 25 m. For the boundary-layer depth estimate, we distinguish between clear-sky and cloud-topped boundary-layers.

370   For clear-sky, relatively increased SNR values are usually connected to an increased amount of aerosol particles in the air. Convection usually enhances the transport of aerosols (Kunkel et al., 1977) and hence aerosol particles are usually more numerous in the convective boundary layer than in the free atmosphere aloft. Hence, at the border between boundary layer and free atmosphere, usually a strong decrease of SNR is observed. The height, at which we identify the strongest decrease of SNR with height is therefore estimated to be the "clear-sky" or "dry" boundary-layer height (m.a.s.l.). We define the clear-sky (or

375   "dry") boundary layer depth as the distance between the surface and the clear-sky boundary-layer height.

For atmospheric conditions, where convective clouds form, we expect the SNR to rapidly increase at the cloud base, as cloud droplets reflect the lidar beam even stronger than aerosol particles. Usually the lidar beam is absorbed after it penetrates a few range gates into the cloud and SNR strongly decreases again. During convective conditions with clouds, we assume the convective cloud-base height to be the upper limit of the boundary layer. We identify the cloud-base height at the altitude, where

380   SNR increases the strongest with height. We define the cloud-topped boundary-layer depth as the distance from the surface to the cloud-base height.

5.2 Turbulent surface heat fluxes

The eddy covariance instrumentation of the SEBS, utilized in both campaigns, provides measurements of the three dimensional wind vector, (u, v, w) (m s^{-1}), the sonic temperature, T_s (°C), and the specific humidity, q (kg kg^{-1}), in 20 Hz time resolution.

385   From the time series of w, T_s, and q, we extract the fluctuations w', T_s', and q' by removing the 30 min average from the measured time series. Then we estimate the 30 min averaged sensible heat flux, H_s (based on Stull, 1988):

$$H_s = \rho_{air} \cdot c_p \cdot \overline{w'T_s'} \tag{9}$$

with the heat capacity of air c_p = 1003.5 J kg^{-1} K^{-1} and the covariance of w' and T_s' averaged over a 30 min interval. We further estimate the 30 min averaged latent heat flux, H_e (based on Stull, 1988):

390    $$H_e = \rho_{air} L_v \cdot \overline{w'q'} \tag{10}$$

with the density of air, $\rho_{air} \approx 1.25$ kg m^{-3} and the latent heat of water $L_v = 2264.705 \cdot 10^3$ J kg^{-1}. The covariance of w' and q' is also averaged over the 30 min interval.

5.3 Flux Richardson number

In the unstably stratified boundary layer, the source of turbulence generation is either buoyancy or shear. The dimensionless ratio

395   of these two terms is defined as Richardson number. With our setup, the assumption of horizontal homogeneity, and neglecting subsidence, we can estimate the near-surface flux Richardson number, Ri_f (based on Stull, 1988):

$$Ri_f = \frac{-\frac{g}{\overline{\theta}} \cdot \overline{w'T_s'}}{|\overline{u'w'}\frac{\partial \overline{u}}{\partial z}| + |\overline{v'w'}\frac{\partial \overline{v}}{\partial z}|} \tag{11}$$

Where $g = 9.81$ m s^{-1} is the earth's gravitational acceleration constant and T_s', u', v', and w' are fluctuations relative to the 30 min average values $\overline{u}$, $\overline{v}$, $\overline{w}$ and $\overline{T_s}$ of the series measured by the SEBS. The sonic anemometer was installed at 3 m above the

400   surface and we assume $\overline{\theta} \approx \overline{T_s}$. The 30 min average vertical gradients, $\frac{\partial \overline{u}}{\partial z}$ and $\frac{\partial \overline{v}}{\partial z}$ are estimated from the profile measurements of $\overline{u}$ and $\overline{v}$ (gradient between cup anemometers and wind vanes installed at 2 m and 4 m).

Only for negative Ri_f, turbulence is generated by buoyancy, while for positive Ri_f buoyancy suppresses turbulence. For $Ri_f \approx$ -1, production of turbulence is balanced between buoyancy and shear, while buoyancy dominates the turbulence generation for $Ri_f <$ -1.

5.4 Convective updraft location

Buoyancy is also the generating mechanism for the convective circulation, which represents the largest eddies in the boundary layer. Convective (buoyant) motion is initiated due to horizontal density anomalies (see i.e. Jeevanjee and Romps, 2015). Locally reduced density at the surface (e.g. by a local temperature increase) results in upward motion of air (buoyant updraft), which is compensated by a horizontal flow towards the updraft region (horizontal convergence). Consequently, we can utilize the retrieved velocity fields of $u(x, z)$ and $w(x, z)$ to identify the presence and the location, x_{up}, of a convective updraft. Generally two conditions need to be met within the lowest hundreds of m for the presence of a convective updraft at x_{up}: A sufficient updraft velocity $w(x) > 0.5 \text{ ms}^{-1}$; and a negative horizontal divergence $\frac{\Delta u}{\Delta x}(x) < 0 \text{ s}^{-1}$. As an additional condition, turbulence generation should not be suppressed by buoyancy ($Ri_f < 0$) during the corresponding time.

6 Two convective show cases

We demonstrate the potential of dual-lidar observations and retrieval for studying convection on the basis of data collected during two convective days. Each day corresponds to one of the campaigns on Vaksinen and Starmoen airport, respectively. The cases represent a variety of scan configurations, surrounding terrain, and meteorological conditions. Considering the challenges met during the two campaigns (see Sect. 2.4), the two days of choice (28 May 2021 and 29 July 2022) provide the most robust observations, namely those with most favourable convective conditions and highest data availability during each of the campaigns. It should be noted, that these two examples are a proof-of-concept for the potential of the dual-lidar approach to study convection and that the presented findings are not valid for convection in general.

6.1 Meteorological conditions and energy balance

Though obtained in May 2021 and July 2022 at different locations, the incoming shortwave radiation, $SW_\downarrow$ (W m^{-2}), is of similar magnitude for both evaluated days (clear-sky: $SW_{\downarrow,max} \approx 750$ W m^{-2}, shown in Figure 6). Both cases show a diurnal cycle in temperature, humidity and wind, which is slightly lagged with respect to the $SW_\downarrow$ series. Compared to the case shown for the Vaksinen site, the near surface wind is slightly weaker and the diurnal temperature amplitude is larger at the Starmoen site. As a consequence, the turbulence generation during hours of net radiative forcing is mainly buoyancy dominated ($Ri_f < -1$) at Starmoen, while at Vaksinen turbulence generation is rather balanced between buoyancy and shear ($Ri_f \approx -1$). Despite the different forcing mechanisms for turbulence generation, the sensible and latent turbulent surface heat fluxes are of comparable magnitude for both cases displayed in Figure 6.

Throughout both days, we observe a net radiative forcing of up to 490 W m^{-2} at the Vaksinen site and up to 460 W m^{-2} at the Starmoen site (see Fig. 6). The latent and sensible heat fluxes make up for ca. 55% and ca. 60% of the net radiation forcing at the Vaksinen and at the Starmoen site, respectively. A maximum residuum of ca. 225 W m^{-2} at Vaksinen and 180 W m^{-2} at Starmoen remains around the period of peak net radiative forcing. The main part of this residuum is usually compensated by the ground flux (not measured here), which can reach values in the order of a few hundreds of W m^{-2} (e.g. Arya, 2001). Still, large
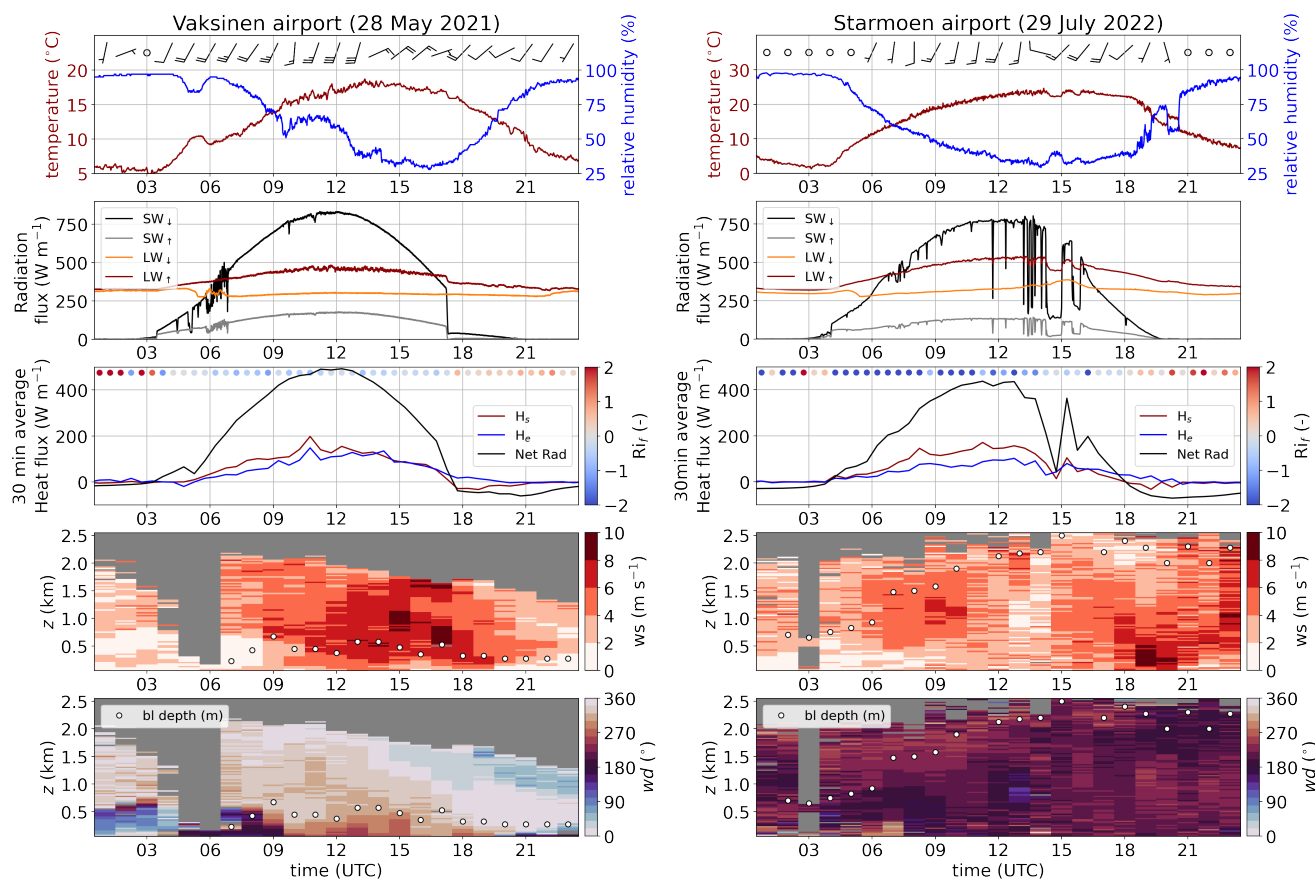
Figure 6. Dirunal cycle of temperature, humidity, and surface wind barbs (short feathers: 1 m s^{-1}, long feathers: 2 m s^{-1}) measured by AWS, incoming ($\downarrow$) and outgoing ($\uparrow$) longwave (LW) and shortwave (SW) radiation, net radiation, turbulent sensible and latent heat fluxes measured and estimated from SEBS measurements, temporal evolution of wind speed, ws, and wind direction, wd, profiles, and boundary-layer depth, bl depth (m above the surface), from lidar observations during two convective days. Left panels: observations at Vaksinen airport (28 May 2021) and right panels: observations at Starmoen airport (29 July 2022)

convective eddies, which are near-stationary over the averaging period of the turbulent flux (30 min) may contribute a substantial part to the energy transport away from the surface. The contribution of such large eddies is not necessarily captured by the turbulent surface heat fluxes. With the dual-lidar setup, on the other hand, we can get a qualitative estimate on the larger-scale flow patterns and their evolution.

440   The wind speed and direction profiles reconstructed from the DBS scans and the boundary-layer depth estimated from SNR profiles based on composites of all RHI scans already give a good overview on the pre-dominating state of the circulation over the two chosen days. Similar to the surface wind, wind speed is also increased throughout the whole profile at the Vaksinen site compared to the Stamoen site, in particular during the convective hours of the day (Fig. 6). Wind direction changes substantially both in time and with altitude at the Vaksinen site, turning from southerly to south-westerly direction (almost parallel to the

445   airstrip) in the boundary layer during the convectively active hours. Above the boundary layer, wind direction turns towards north and later on towards east. At Starmoen, wind is mostly from south to south-westerly directions over the whole day and observed altitude range, which is almost perpendicular to the airstrip. The most striking difference between the two cases is the large difference in boundary-layer depth. At the Vaksinen site the boundary layer is quite shallow and reaches only a few hundreds of m depth. At Starmoen, on the other hand, the boundary layer rises up to more than 2000 m over the course of the

450   day, yielding also the possibility of comparably deeper convective circulation.

6.2   Dual-lidar approach for a clear-sky case of convection

We demonstrate the reconstruction of the flow field (u, w) in the cross-section between the two lidars from the temporally interpolated v_r fields (one snapshot) during the Vaksinen airport campaign (28 May 2021 between 15 and 16 UTC), which are displayed in Figure 7. The interpolated v_r values in the RHI scans (Fig. 7a-f) correspond to the time step which is exactly at the

455   middle of each individual scan configuration period.

Despite a time difference of 10 minutes and 20 minutes in between the different scan configurations, all retrieved fields of u and w indicate the presence of a convective updraft, triggered at around $x = 200$ (Fig. 7g-l). With the retrieved u and w fields and on the basis of the method introduced in Sect. 5.4, we estimated x_{up}, where the convective updrafts originate at the surface. Figure 8 visualizes the identification process applied to the three retrieved u and v fields which are presented in Figure 7. Here,

460   the height-averaged w (over the lowest 150 m) reaches a local maximum ($w > 0.5\,\mathrm{m\,s^{-1}}$) and u converges (reverses sign from positive to negative with increasing x: $\Delta u / \Delta x < 0$) within the grey shaded area for the three tested scan configurations. This area is in fact located around the $x = 200$ mark (Fig. 8).

For all three scan configurations the maximum w and minimum $\Delta u / \Delta x$ fall almost into the same point (x_{up}) at $x = 230$ m, $x = 200$ m, and $x = 200$ m, respectively. Given the meteorological background conditions (see Sect. 6.1 and Fig. 6), buoyancy

465   contributes to the turbulence generation ($Ri_f < 0$) and can be considered the main driver for the observed circulation patterns. Horizontal velocity divergence is expected at the upper edge of the convective updraft to compensate the upward motion of air. A divergent behaviour is, in fact, evident in all three retrieved u fields (Fig. 7j-l), however much weaker than the near-surface convergence. Similar as observed by Kunkel et al. (1977) the updraft is attached to the surface and has more of a plume-like character, while at higher altitudes "bubbles" of increased vertical velocities seem to detach.

470   The near-surface, horizontal velocity convergence around $x = 200$ m is already well captured by the v_r fields, obtained by lidar-37, which is located at $x = -335$ m (Fig. 7a-c). The lidar's beam is oriented almost horizontal relative to the near-surface flow field, relevant to the convective updraft and convergence region. Here, angular, or spatial resolution do not matter, since even the lowest angular resolution of 2.0° (Fig. 7c) sufficiently captures all relevant features of the horizontal flow. Lidar-40 is located at $x = 335$ m, which is comparably close to the convective updraft region around $x = 200$ m, for all three scan

475   configurations. The region of horizontal velocity convergence, which is not exactly located above lidar-40, is also evident in the horizontal pointing beams (Fig. 7d-f, j-l). Yet here, the updraft strongly contributes to the v_r signal of the vertical or close to vertical pointing beams (Fig. 7d-i).
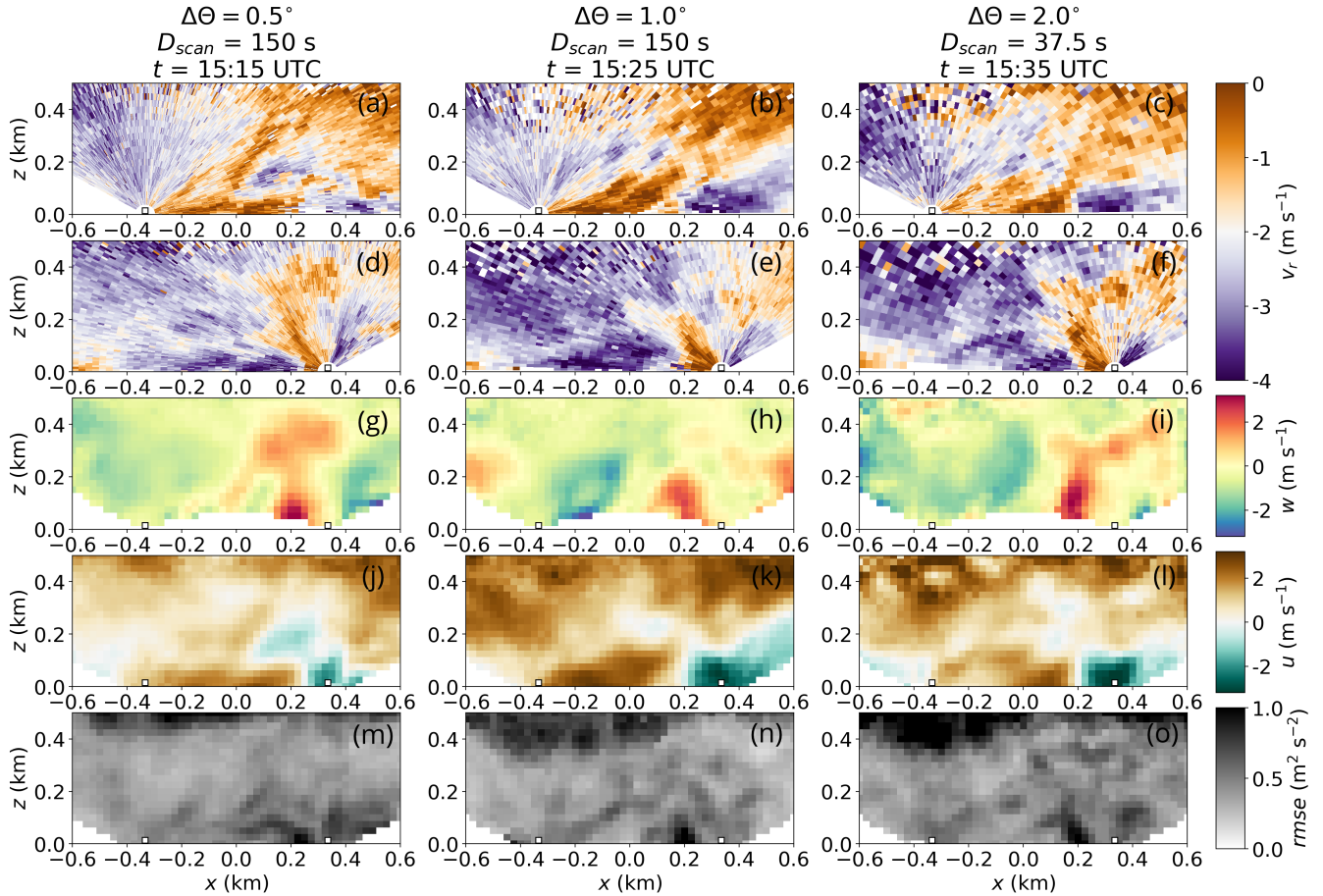
Figure 7. Filtered and temporally interpolated v_r observations, retrieval, and retrieval error obtained for 28 May 2021 between 15 UTC and 16 UTC at Vaksinen airport. The location of the utilized lidars is indicated by white squares with a black border just above the surface, with $lidar_1$ in the negative and $lidar_2$ in the positive x domain in each of the subplots. The three columns correspond to the three different scan configurations with configuration specific $\Delta\theta$, D_{scan} and t (instantaneous cross-section). Each row corresponds to one relevant variable. 1. row (a-c): processed, instantaneous v_r fields from lidar-37 (here $lidar_1$); 2. row (d- f): processed, instantaneous v_r fields from lidar-40 (here $lidar_2$); 3. row (g-i): retrieved w field; 4. row (j-l): retrieved u field; 5. row (m-o): retrieval $rmse$ field.

Within the convectively active region, the $rmse$ is remarkably similar for all three scan configurations (7m-o). It is increased close to the updraft region near to the surface ($x = 200$, $z < 100$). The main cause for this increased $rmse$ is an erroneous estimate of the large w component in the near-surface region. The w contribution to the observed v_r is negligible, since here both lidars observe v_r with predominantly horizontal pointing beams (ill-posed in w). This issue was already addressed by removing any ill-posed w values from the retrieved field (see Sect. 4.2). Above the downdraft region, a larger area of increased $rmse$ is present for all three scan configurations (upper left corner of the displayed retrieval grid). Here SNR values are decreased (not shown), hence fewer v_r values are available for the retrieval. The boundary-layer depth is horizontally in-homogeneous and in
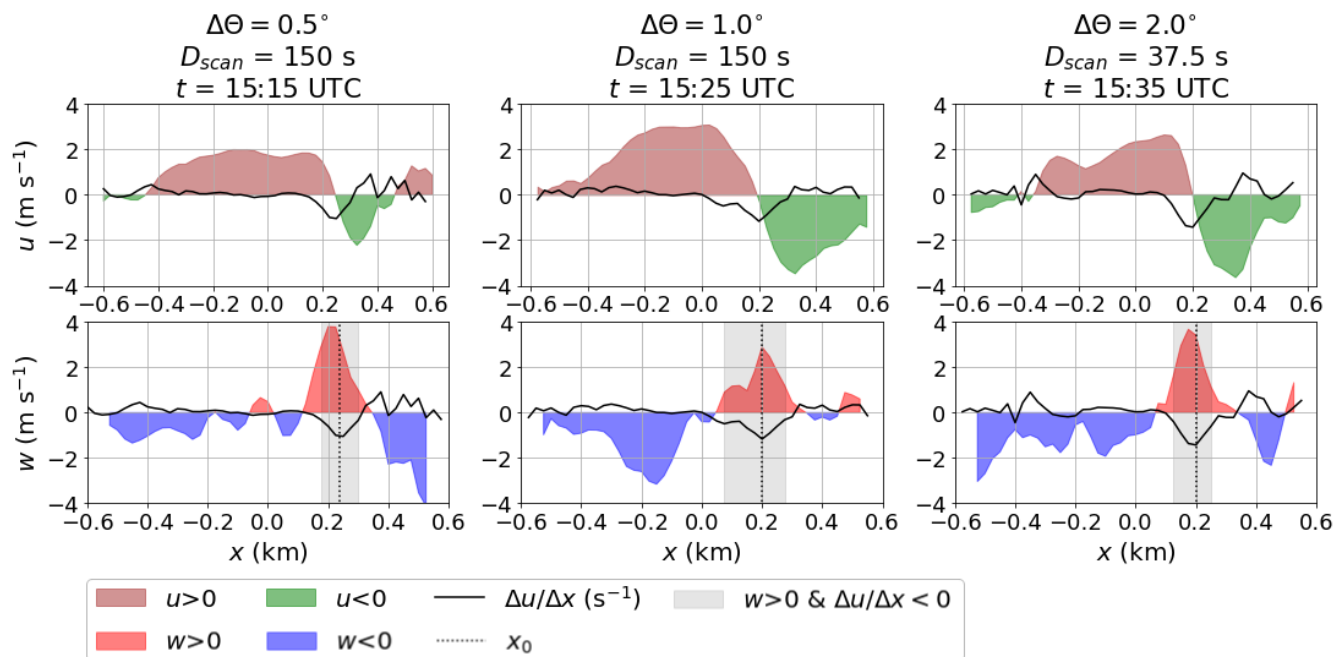
Figure 8. Averaged, near surface (≤ 150 m) horizontal divergence, 1. row: u and 2. row: w estimates to visualize the identification process for the near-surface updraft location, x_0. The three columns correspond to the three different scan configurations with configuration specific $\Delta\theta$, D_{scan} and t (instantaneous cross-section).

particular increased above the updraft. Hence, the connective updraft directly drives the boundary-layer deepening, while the downdraft entrains clear air from the free atmosphere, where uncertainty in the lidar retrieval rapidly increases. Due to its rapid transport of aerosols through the atmosphere, the connective updraft is consequently well fit to be observed with a Doppler lidar.

6.3 Development of a cloud-topped convective structure

During the Starmoen campaign, we captured a convective day with comparable temperature and humidity development, as well as radiation and turbulent fluxes (Fig. 6). The main differences to the convective day investigated from the Vaksinen campaign is the increased depth of the boundary layer and the formation of convective clouds in the afternoon. The presence of clouds at Starmoen airport on the day of interest is evident from the periods of strongly reduced values of $SW_{\downarrow}$ during the afternoon (see Fig. 6). From ca. 13 UTC until 14 UTC, $SW_{\downarrow}$ rapidly fluctuates between diffuse (cloud-shadowed) and near-clear sky values indicating the presence of non-stationary and rather small-scale clouds. From ca. 14 UTC to 15 UTC, the pyranometer was continuously shadowed by a larger, more stationary cloud (see Fig. 9). At the time the photo in Figure 9 was taken, the shadow of the cloud covered the entire airfield, though the lidars only capture a finite slice of this cloud within the scanned cross-section as a strong, local increase in SNR at the cloud base.

Figure 9. Cloud observed over Starmoen Airport on 29 July 2022 at 14:23 UTC

We estimate the fields of u and w in the vertical cross-section between the lidar on the basis of instantaneous RHI scans (see. Sect. 3.2) every 4th minute from 14:04 UTC until 14:32 UTC. These fields, as well as the corresponding streamlines and an indication of the cloud base as SNR contours (SNR > -10 dB) are displayed in Figure 10.

The first row of velocity fields and streamlines (14:04 UTC, Fig.10a-c) features only weak signs of convection. Both u and w are small overall, except for a small pattern of increased w at the edge of the retrieval grid. Though u and w are organized in clusters of positive and negative values (updraft, downdraft and horizontal convergence and divergence), the corresponding streamlines indicate a predominantly turbulent flow with local, small-scale fluctuations and no predominant convective pattern. An indication of a cloud is visible above the weak updraft region, which possibly is a remnant of an earlier convective circulation.

The subsequent fields, displayed in Figure 10d-f corresponding to 14:08 UTC, show an intensification of both the horizontal and vertical velocity clusters, which allow a clear distinction into up- and downdraft. Here, the maximum updraft velocity, $w^{\uparrow}_{max}$, reaches 2.1 m s^{-1}. Also the streamlines imply a clearer organisation of the flow, with less impact of localized and small-scale turbulence indicating the onset of an new, emerging convective circulation. The updraft terminates at the height of the cloud base which is indicated in Fig. 10f and hence spans the whole depth of the cloud topped boundary layer. However, there is no indication for the cloud to be present above the downdraft region within the retrieval grid. Note, that the availability of v_r is greatly reduced within the cloud and u and w estimates are less reliable within and above the cloud base.

The panels corresponding to the next time step (14:12 UTC) displayed in Figure 10g-i show a further intensification of the updraft velocity ($w^{\uparrow}_{max} = 2.9$ m s^{-1}) and a clearer distinction of negative and positive velocity clusters in the horizontal wind component (along the lidar cross-section). The updraft (Fig. 10g) is focused into a narrow stream closer to the surface, which widens and increases in strength with increasing altitude and has a more plume-like character, as also observed by (Kunkel et al., 1977). The stream maintains a core of maximum updraft velocity above the origin region at the surface. A second, weaker core of positive vertical velocity, separated at the surface, merges into the updraft cluster at a higher altitude ($z = 1$ km), possibly
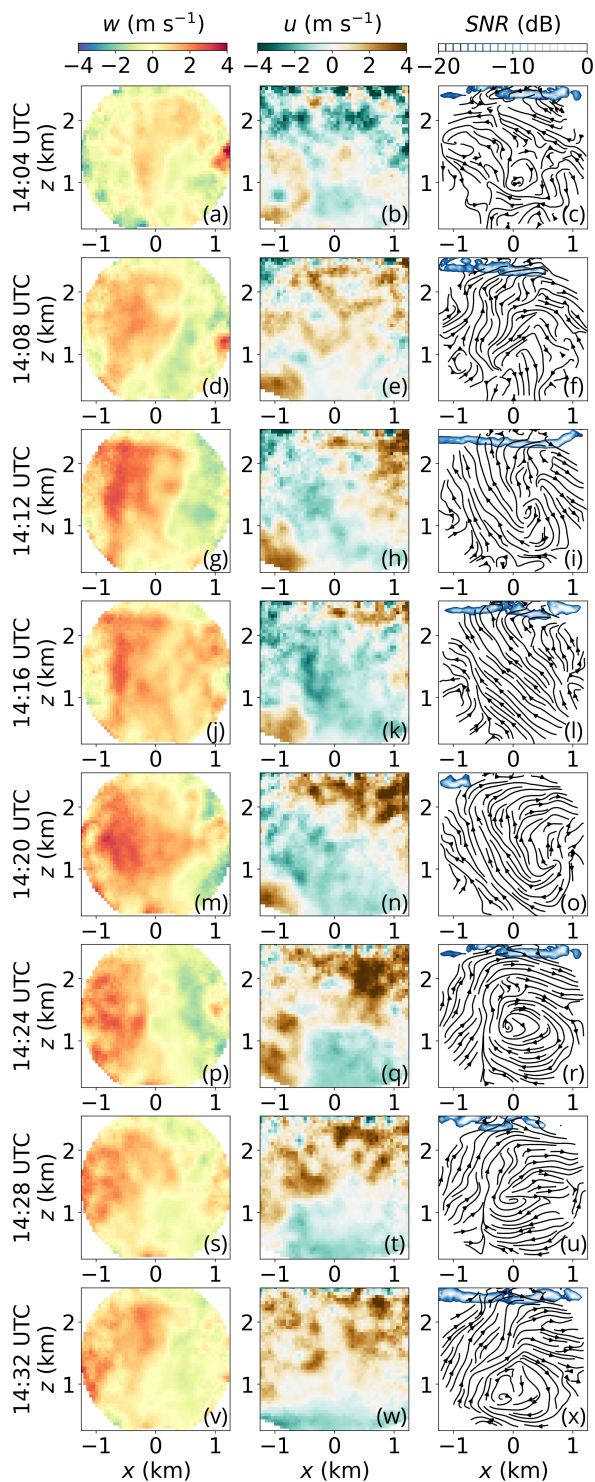
Figure 10. Temporal evolution of convection on 29 July 2022 at Starmoen Airport. 1. column: retrieved w field, 2. column: retrieved u field, 3. column: streamlines and SNR (cloud back-scatter)

contributing to the updraft's widening at this level. Here, the horizontal velocities (Fig. 10h) show a clear converging pattern
at the location, where the main updraft core emerges from the surface, but none for the secondary and weaker updraft. In the
upper part of the thermal ($z > 1$ km) the horizontal velocity clusters reverse in sign compared to the lower part, corresponding to
horizontal divergence of the updraft, in line with convective theory. The streamlines corresponding to the convective circulation
are clearly defined and indicate the presence of a continuous stream of air upwards. Interestingly, the width of the convective
stream is conserved over the altitude range where horizontal convergence dominates. Hence, the converging velocity field is a
substantial contribution to the convective circulation. The horizontal divergence in the upper part of the thermal contributes to
the widening of the thermal, also visible when following the streamlines. The cloud base is mainly located above the updraft
region at $z = 2.4$ km, where horizontal velocity begins to dominate the vertical velocity and the streamlines diverge. Above the
downdraft cluster, the cloud base is comparably increased (above 2.5 km). The thermal slightly tilts towards the left side of the
projected velocity field.

At 14:16 UTC, the updraft cluster (Fig. 10j) widened substantially in comparison to the preceding time step (Fig. 10g). Here,
the updraft patch and the cloud (Fig. 10j,l) cover nearly the entire width of the cross-section, which now is too narrow to document
the complete convective circulation pattern (up-and downdraft). The core of maximum updraft velocity ($w^\uparrow_{max} = 2.8$ m s^{-1}),
which emerges from the surface and extends continuously up to the cloud base at $z = 2.4$ km, still dominates the left-hand side of
the cross-section. In contrast, the right-hand side of the cross-section features a more locally increased vertical velocity clusters,
possibly corresponding to individual bubbles released from the surface. Strong horizontal velocity convergence (Fig. 10k) is still
evident close to the surface ($z < 0.8$ km), where the thermal core releases around $x = -0.5$ km. The horizontal divergence is
almost exclusively present at the cloud base, while the wide updraft region between $z = 0.8$ km and $z = 2.4$ km is dominated by
negative horizontal velocity. As a result, the streamlines are even stronger tilted towards the left-hand side of the cross-section,
than during the proceeding time step.

At 14:20 UTC (Fig. 10m-o), the thin core of maximum velocity vanished and the updraft looses it's predominantly plume-like
character. Instead, a larger cluster of increased vertical velocities emerged ($w^\uparrow_{max} = 3.2$ m s^{-1}), which does not clearly originate
close to the surface. Overall, the updraft cluster does not extend as far to the right-hand side of the lidar retrieval cross-section
as the preceding time step. Yet, the location of maximum, near-surface, horizontal convergence remains at approximately the
same spot ($x = -0.6$ km). Horizontal divergence is already present at lower altitudes, from $z \approx 1.7$ km up to the comparably
elevated cloud base at $z = 2.5$ km. The streamlines are still tilted towards the left-hand side, yet already showing a much stronger
contribution of horizontal velocity at lower levels ($z = 1.7$ km) up to the cloud base.

At 14:24 UTC (Fig. 10p-r), the part of the vertical velocity cluster which is captured by the lidars, covers solely the left-hand
side of the cross-section. The right-hand side is occupied by a downdraft cluster (both up- and downdraft clusters are not tilted
and are oriented almost perpendicular to the surface). The overall vertical velocity strength ($w^\uparrow_{max} = 2.8$ m s^{-1}) is decreased in
comparison to the proceeding time step. Also, no distinct stream from the surface to the cloud base is present. The location of
maximum horizontal convergence (x_{up}) is still around $x = -0.6$ km, yet extends higher up ($z = 1.5$ km) and rises perpendicular
to the surface in contrast to the time steps evaluated before. Also, the streamlines are almost upright at x_{up}. Horizontal inflow

near the surface up to $z = 1$ km, and horizontal outflow from the thermal below the cloud base covers a larger horizontal distance
than observed in the earlier stages of the convection.

555   At 14:28 UTC (Fig. 10s-u), the weak remains of the updraft cluster ($w^{\uparrow}_{max} = 2.5$ m s^{-1}) are further pushed out of the
lidar cross-section (mainly in the lower part). Also, the horizontal velocity gradient and hence the strength of the convergence
decreases, yet the streamlines still converge and are close to perpendicular to the surface around $x = -0.6$ km. Here, the buoyant
forcing of the convection begins to break down and only inertia maintains the vertically opposing u field and horizontally
opposing w field. Also, the cloud is still present, yet with no further fueling from below, it will eventually break down, or will be
560   advected away from the site with time (see Fig. 6)

    The last row of displayed panels (14:32 UTC, Fig. 10v-x), documents a continuation of the weakening (break-down) of
the convective cluster, which already started in the preceding time step ($w^{\uparrow}_{max} = 2.3$ m s^{-1}). Here, also the convergence and
divergence are not captured within the lidar-observed horizontal velocity field anymore. Instead, horizontal velocity of the
opposing signs dominates the upper and lower part of the lidar cross-section, respectively. As a consequence, the streamlines tilt
565   toward the right-hand side of the lidar cross-section with increasing altitude, opposite to the tilt which we observed at the onset
of the convective circulation. The boundary-layer reached its peak during this hour. Afterwards, radiative forcing, turbulent heat
fluxes, and turbulence generation by buoyancy decrease (Fig. 6) and connective activity ceases for that day.

7   The potential of the dual-lidar setup and retrieval

We tested the potential of a setup combining two scanning lidars, to resolve and characterize atmospheric convection in a
570   vertical plane. While the setup will at best be able to retrieve the two-dimensional evolution of the three-dimensional convective
flow, this does not necessarily reduce the potential of this approach, as convective circulation is often rather symmetric around
its vertical axis (updraft or downdraft), given calm background wind speed conditions (e.g. Emanuel et al., 1994). In case of
sufficient background wind, the convective structure will be tilted and the cross-section should ideally be oriented parallel to the
wind direction to capture the vertical extent of the convective circulation. Furthermore, to interpret the absolute strength and
575   width of the convective up- or downdraft, the cross-section should pass through the core of the convective structure.

    As the lidars are rather immobile, it is not realistic to adjust the setup to each state of the convective circulation. Hence, it is
beneficial to orient the lidars according to the dominant wind direction during convective conditions. To ensure that the setup
frequently captures convection, it is also of advantage that the cross-section is placed over surfaces that are likely to trigger
convection. For our setup along the airport runways, we experienced a satisfying hit-rate of representative convective circulation
580   patterns, even though wind and surface conditions were not necessarily optimal (e.g. wind direction was almost perpendicular to
the orientation of the retrieval plane at Starmoen and a lake is located in very close to the Vaksinen site). A significant advantage
for the sites at the selected airfields was that we were able to use the insights from the local sailplane pilots about convective hot
spots prior to the campaign. Given the location, our observation of the flow field above the airport were of great relevance the
pilots, even during non-convective conditions.

585   Reducing the errors and complications connected to the setup has a substantial impact on the potential of the dual-lidar retrieval. A thorough azimuth calibration of the utilized lidars following Leosphere (2022) prevents unnecessary amplification of out-of plane v_r errors in the retrieval (see. Stawiarski et al., 2013). While synchronisation of scan schedules is only of secondary importance (in contrast to Röhner and Träumner, 2013), time synchronisation of the lidar-internal clocks is critical. Wrongly matched time stamps are generally hard to identify and correct, yielding amplified errors in v_r retrieval.

590   Generally, the dual-lidar retrieval is quite sensitive to erroneous v_r input, as also discussed by Stawiarski et al. (2013). We found that pre-processing the RHI scans before retrieval has a positive impact on the error reduction and hence on the potential of the dual-lidar approach. The error in v_r connected to noise and erroneous features can be up to an order of magnitude larger than actual values of v_r. As RHI scans are particularly prone to range-folded ambiguities (Bonin and Brewer, 2017), it is crucial to remove these before further processing.

595   For the RHI observations, the DBSCAN filter (adapted from Alcayaga, 2020) proves to be more effective and accurate than the conventional SNR threshold filter. Applying the DBSCAN filter strongly increases the potential of the dual-lidar observations for various conditions. Further processing, in form of temporal interpolation of the RHI scans additionally reduces the error compared to using the obtained RHI scans, where θ is dependent on t. From the interpolated scan series, instantaneous scans can be extracted, which reduces the necessity of exact scan schedule synchronisation. Also, the interpolation has a larger impact

600 on the temporal error reduction than doubling the temporal resolution of the scans. Since temporal interpolation still has a "blurring" effect on the retrieval, similar to using a temporal radius (see. Newsom et al., 2008), it is still beneficial to use a high sampling rate for the scans as the base for the interpolation.

    We implement and apply a retrieval algorithm that follows a similar methodology as well-established retrievals for overlapping dual-lidar scans (e.g. Newsom et al., 2008; Träumner et al., 2015; Haid et al., 2020). These methodologies are, however, more

605 commonly applied for horizontally overlapping scans than for RHI scans. The main challenge in the retrieval is to accurately project and combine the v_r values from two different polar coordinate systems to a common cartesian coordinate system. We find the best estimate of u and v by solving an over-constrained equation system for each Cartesian point, containing several v_r values of both lidars. This reduces the impact of outliers and additionally yields a retrieval error estimate that serves as a measure of confidence for the retrieval in each point.

610   The retrieval yields a promising representation of the convective circulation for two convective cases. In both cases, convection is well resolved over the entire depth of the boundary layer. In particular, the convective updraft and a clear evidence of horizontal velocity convergence in the lower part of the convective circulation is captured. This also allows to identify secondary convective parameters, e.g., the origin of the updraft close to the surface as well as the strength and the size of the updraft.

    During the onset and within the early phase of the cloud-topped case with a deep boundary layer, buoyancy forces the

615 convective, plume-like updraft. After the internal convective circulation established a sufficient updraft together with a convergent horizontal flow at the surface and a divergent horizontal flow aloft, inertial forcing starts to dominate and maintain the circulation (see e.g. Jeevanjee and Romps, 2016). We observe a widening and weakening of the convective updraft, as entrainment of environmental air and drag forces counteract the effective buoyancy, as also proposed by Jeevanjee and Romps (2016). At this point, the updraft looses it's plume-like characteristics. We also observed a plume-like attachment of the updraft to the surface

620   during the clear sky case, similar to Kunkel et al. (1977). However, the upper part of the updraft showed signs of detachment of individual "bubbles" with increased vertical velocity.

It is remarkable for this shallow boundary layer, where only smaller scale convection dominates, that even the lowest angular resolution is sufficient to resolve these characteristic features of the convective circulation. We face a bigger problem to capture the entirety of a very large scale convection that exceeds the boundaries of the retrieval grid in the cloud-topped case. Also,

625   the retrieval becomes less reliable above the cloud base, as the lidar beams can only penetrate a few range gates into the cloud and the data availability drops rapidly. The dual-lidar retrieval is therefore mostly relevant for the dry part of the convective circulation.

We utilize several scan configurations with various temporal and spatial resolutions. During the first campaign at the Vaksinen site we even tested three different scan configurations. The comparison of the different scanning patterns proved to be challenging,

630   as we cannot be sure whether the differences in observed data are due to changing flow conditions or changes of the scan configuration. In particular, the 10 min scanning interval, which yields an acceptable uncertainty of the changes related to the convective flow field, turned out to be too short for the scan configurations with long D_{scan} (150 s) and did not achieve representative error statistics. To sufficiently compare the scan resolutions, simultaneous observations by an additional lidar would be required. Yet, we found a solution by artificially decreasing the highest obtained temporal resolution, which yields a

635   representative indication of impact of the temporal resolution on the error.

For the evaluated cases, all convectively relevant scales are well represented, even by the lowest spatial resolution tested within the retrieval grid, which is still in close vicinity of the lidars. It is therefore reasonable to use high temporal resolution, even at the cost of spatial resolution or, if the aerosol concentration allows, at the cost of T_{scan}.

It was also not easy to find continuity between the consecutive series of changing scan configurations, as the temporal

640   interpolation is only able to produce an entire instantaneous RHI scan after one complete scan. We can only sufficiently resolve the full temporal development of a convective circulation for a continuously sampled series with constant temporal and spatial resolution. As observed for our cloud-topped case, the development of a convective circulation can have a lifecycle of the order of several tens of minutes. But there is also an indication for longer lasting convective patterns for the smaller convective scales obtained at the Vaksinen site.

645   The two-dimensional wind field retrieved from the dual-lidar setup of two convective cases effectively illustrates the potential of the dual-lidar approach to study convection. With the setup, we can clearly characterize the convective flow field, as well as secondary convective properties, such as the triggering location of the convective updraft close to the surface, the strength of the convective updraft, and the boundary-layer depth. The two cases already yield insights into the characteristics of convection during clear-sky and cloud-topped boundary-layer conditions. In both cases, we observe that the convective

650   circulation spans the entire depth of the boundary layer. Consequently, convection is contributing substantially to the transport of heat, moisture, momentum, and aerosols, as well as to boundary-layer deepening, or is at least responsible for the maintenance of the boundary-layer depth.

The dual-lidar retrieval complements valuable insights to the surface-based measurements, by quantifying the substantial differences in the deepening of the boundary layer by the convective circulation for the case at Vaksinen compared to Starmoen.

655 One potential explanation is the different geographic setting of the locations. The Vaksinen airport is located in a local valley with rather steep topography of approximately 300 m height. This topography potentially enhances the accumulation of cold air in the valley and the development of a nocturnal low-level temperature inversion. In addition, Vaksinen airport is located relatively close to the North sea, which is a large body of comparably low temperature in May. Cold-air advection from the sea creates an internal boundary layer (Garratt, 1990), which can also contribute to the maintenance of a strong, low-altitude

660 temperature inversion, which is hard to penetrate even for strong updrafts, as observed at the Vaksinen site.

The Starmoen site is much flatter and located far away from any water body of comparable size and the case features a deeper residual layer from the preceding day. As energy input near the surface and turbulent fluxes increase, convection continuously deepens the boundary layer. The strength of the convective updraft is not stronger compared to the one observed at the Vaksinen site, indicating that there is a weaker inversion. The potential of a deeper boundary layer is indicated (more negative Ri_f), but

665 not possible to quantify without complementing temperature profiles.

With the DBS scan included into the lidar schedules for 10 min each hour, we are able to gain an estimate of the mean profile of the three-dimensional wind. This profile indicates how parallel the flow is towards the evaluated dual-lidar cross section. Yet, from the dual-lidar retrieval we can clearly observe, that the flow during convective conditions is very complex and non-homogeneous already on small horizontally scales, which is a requirement for an accurate DBS retrieval. As a consequence,

670 the DBS retrieval may not sufficiently capture the profile, in particular with increasing separation of beams with height. Another problem of the DBS scan is that it introduces a discontinuity in the retrieved dual-lidar cross-section time series. In the worst case, the DBS scan is scheduled during a crucial period in the evolution of the convective circulation. As the quality of the DBS retrieval is uncertain, an alternative solution to sample the profile of the three-dimensional wind, which does not interrupt the continuity of the overlapping RHI scans would be an improvement. A third lidar that scans perpendicular to the dual-lidar setup,

675 creating a "virtual tower" (see Calhoun et al., 2006) could achieve this for example.

The complementing ground-based measurements, such as used here are beneficial to the setup. They can enhance the process of identifying relevant periods for convection and give some indication on the strength and depth of the convection (e.g. Ri_f, or a parameter such as the convective velocity scale $w_* \sim \overline{w'\theta'}$ as discussed by Träumner et al., 2011). However, to learn more about the character and physics of the convective boundary-layer and evolution of convective circulation,

680 more sophisticated measurements are needed. Background profiles of temperature, humidity, and wind as well as profiles simultaneously measured within the thermal to complement the flow field estimates of the dual-lidar approach could significantly improve our understanding of convection, e.g. when evaluated in an empirical model such as introduced by Pálenik et al. (2020). The gLidar project, actually aims to achieve such collocated observations.

8   Conclusions

685 We demonstrated that our proposed dual-lidar setup has a promising potential to sample and characterize the dynamic properties of atmospheric convection.

We showed that pre-processing the observed v_r with a novel cluster filtering approach and utilizing instantaneous dual-lidar scans obtained from temporal interpolation, increases the data availability and strongly reduces errors yielding a valuable retrieval of the convective flow field. We sufficiently resolved the details of the convective circulation at all tested angular resolutions and conclude that it is beneficial to prioritize a high temporal resolution, over a high angular resolution.

We presented two cases, highlighting the large potential of our dual lidar setup to gain additional insight about the convective evolution of the boundary layer. These observations significantly complement the more commonly used ground-based measurements. Our proposed dual-lidar approach yields the convective flow field, from which we can quantify several relevant convective parameters, such as the origin, depth, width, and strength of the convective updrafts. Combining the proposed dual-lidar approach with the observation of additional profiles of temperature and humidity in- and outside of the convective updraft, offer the potential to gain a deeper physical understanding of the dynamic processes inherent to convection.

Code and data availability. All code, raw and processed data can be provided by the corresponding authors upon request.

Author contributions. CD, JP, TS and JR developed the instrument setup and planned the campaign. CD and JP developed the retrieval and pre-processing code. CD analysed the data and wrote the manuscript draft. JP, TS and JR reviewed and edited the manuscript.

Competing interests. The authors declare that there are no competing interests.

Acknowledgements. The three lidars used in this study are part of the National Norwegian Research Infrastructure OBLO (Offshore Boundary Layer Observatory (OBLO) funded by the Research Council of Norway (RCN) (project number: 227777). The experimental work was supported by funding from Faculty of Mathematics and Natural Sciences at the University of Bergen (Fellesfond for geofysisk forskning). The campaign at Elverum was facilitated by the Research school on changing climates in the coupled earth system (CHESS) funded by RCN (project number: 245854). The authors would like to thank the Aero club in Os and the Ole Reistad Center, the Norwegian Air Sports Federation's national center for gliding, for the possibility to install our instrumentation and for their logistical support and hospitality during the campaigns. Special thanks go to our engineering staff, Anak Bhandari for his work and assistance in campaign planning and realization and Tor Olav Kristensen for the design and assistance in building the remote access solution for the lidar systems.

References

Adler, B., Kalthoff, N., and Kiseleva, O.: Detection of structures in the horizontal wind field over complex terrain using coplanar Doppler lidar scans, Meteorologische Zeitschrift, 29, 467–481, https://doi.org/10.1127/metz/2020/1031, 2020.

Alcayaga, L.: Filtering of pulsed lidar data using spatial information and a clustering algorithm, Atmospheric Measurement Techniques, 13, 6237–6254, https://doi.org/10.5194/amt-13-6237-2020, 2020.

Arya, S. P.: Introduction to Micrometeorology; 2nd ed., Elsevier, San Diego, CA, https://cds.cern.ch/record/1086959, 2001.

Bonin, T. A. and Brewer, A. W.: Detection of Range-Folded Returns in Doppler Lidar Observations, IEEE Geoscience and Remote Sensing Letters, 14, 514–518, https://doi.org/10.1109/LGRS.2017.2652360, 2017.

Brown, A. R., Cederwall, R. T., Chlond, A., Duynkerke, P. G., Golaz, J.-C., Khairoutdinov, M., Lewellen, D. C., Lock, A. P., MacVean, M. K., Moeng, C.-H., Neggers, R. A. J., Siebesma, A. P., and Stevens, B.: Large-eddy simulation of the diurnal cycle of shallow cumulus convection over land, Quarterly Journal of the Royal Meteorological Society, 128, 1075–1093, https://doi.org/https://doi.org/10.1256/003590002320373210, 2002.

Calhoun, R., Heap, R., Princevac, M., Newsom, R., Fernando, H., and Ligon, D.: Virtual Towers Using Coherent Doppler Lidar during the Joint Urban 2003 Dispersion Experiment, Journal of Applied Meteorology and Climatology, 45, 1116 – 1126, https://doi.org/10.1175/JAM2391.1, 2006.

Duscha, C., Barrell, C., Renfrew, I. A., Brooks, I. M., Sodemann, H., and Reuder, J.: A Ship-Based Characterization of Coherent Boundary-Layer Structures Over the Lifecycle of a Marine Cold-Air Outbreak, Boundary-Layer Meteorology, 183, 355—-380, https://doi.org/10.1007/s10546-022-00692-y, 2022.

Emanuel, K. A. et al.: Atmospheric convection, Oxford University Press on Demand, 1994.

Garratt, J. R.: The internal boundary layer — A review, Boundary-Layer Meteorology, 50, 171—-203, https://doi.org/10.1007/BF00120524, 1990.

Geerts, B., Raymond, D. J., Grubišić, V., Davis, C. A., Barth, M. C., Detwiler, A., Klein, P. M., Lee, W.-C., Markowski, P. M., Mullendore, G. L., and Moore, J. A.: Recommendations for In Situ and Remote Sensing Capabilities in Atmospheric Convection and Turbulence, Bulletin of the American Meteorological Society, 99, 2463 – 2470, https://doi.org/10.1175/BAMS-D-17-0310.1, 2018.

Haid, M., Gohm, A., Umek, L., Ward, H. C., Muschinski, T., Lehner, L., and Rotach, M. W.: Foehn–cold pool interactions in the Inn Valley during PIANO IOP2, Quarterly Journal of the Royal Meteorological Society, 146, 1232–1263, https://doi.org/https://doi.org/10.1002/qj.3735, 2020.

Iwai, H., Ishii, S., Tsunematsu, N., Mizutani, K., Murayama, Y., Itabe, T., Yamada, I., Matayoshi, N., Matsushima, D., Weiming, S., Yamazaki, T., and Iwasaki, T.: Dual-Doppler lidar observation of horizontal convective rolls and near-surface streaks, Geophysical Research Letters, 35, https://doi.org/https://doi.org/10.1029/2008GL034571, 2008.

Jeevanjee, N. and Romps, D. M.: Effective Buoyancy, Inertial Pressure, and the Mechanical Generation of Boundary Layer Mass Flux by Cold Pools, Journal of the Atmospheric Sciences, 72, 3199 – 3213, https://doi.org/10.1175/JAS-D-14-0349.1, 2015.

Jeevanjee, N. and Romps, D. M.: Effective buoyancy at the surface and aloft, Quarterly Journal of the Royal Meteorological Society, 142, 811–820, https://doi.org/https://doi.org/10.1002/qj.2683, 2016.

Kunkel, K. E., Eloranta, E. W., and Shipley, S. T.: Lidar Observations of the Convective Boundary Layer, Journal of Applied Meteorology and Climatology, 16, 1306 – 1311, https://doi.org/10.1175/1520-0450(1977)016<1306:LOOTCB>2.0.CO;2, 1977.

745   Lai, T. L., Robbins, H., and Wei, C. Z.: Strong consistency of least squares estimates in multiple regression, Proceedings of the National Academy of Sciences, 75, 3034–3036, https://doi.org/10.1073/pnas.75.7.3034, 1978.

Leosphere: WindCube Scan software suite User Manual Version 20.f, Vaisala France, Tech Park, 6A rue René Razel 91 400 Saclay, France, 2022.

Newsom, R., Calhoun, R., and Ligon, D.: Linearly Organized Turbulence Structures Observed Over a Suburban Area by Dual-Doppler Lidar,
750   Boundary-Layer Meteorology, 127, 111–130, https://doi.org/https://doi.org/10.1007/s10546-007-9243-0, 2008.

Newsom, R. K., Ligon, D., Calhoun, R., Heap, R., Cregan, E., and Princevac, M.: Retrieval of microscale wind and temperature fields from single-and dual-Doppler lidar data, Journal of Applied Meteorology and Climatology, 44, 1324–1345, 2005.

Prein, A. F., Rasmussen, R., and Stephens, G.: Challenges and Advances in Convection-Permitting Climate Modeling, Bulletin of the American Meteorological Society, 98, 1027 – 1030, https://doi.org/10.1175/BAMS-D-16-0263.1, 2017.

755   Pálenik, J.: gLidar project website, https://glidar-project.github.io/, 2022.

Pálenik, J., Spengler, T., and Hauser, H.: IsoTrotter: Visually Guided Empirical Modelling of Atmospheric Convection, https://doi.org/10.48550/ARXIV.2008.10301, 2020.

Röhner, L. and Träumner, K.: Aspects of Convective Boundary Layer Turbulence Measured by a Dual-Doppler Lidar System, Journal of Atmospheric and Oceanic Technology, 30, 2132 – 2142, https://doi.org/10.1175/JTECH-D-12-00193.1, 2013.

760   Siebesma, A. P., Soares, P. M. M., and Teixeira, J.: A Combined Eddy-Diffusivity Mass-Flux Approach for the Convective Boundary Layer, Journal of the Atmospheric Sciences, 64, 1230 – 1248, https://doi.org/10.1175/JAS3888.1, 2007.

Stawiarski, C., Träumner, K., Knigge, C., and Calhoun, R.: Scopes and Challenges of Dual-Doppler Lidar Wind Measurements – An Error Analysis, Journal of Atmospheric and Oceanic Technology, 30, 2044 – 2062, https://doi.org/10.1175/JTECH-D-12-00244.1, 2013.

Stull, R. B.: An Introduction to Boundary Layer Meteorology, Springer, Dordrecht, https://doi.org/https://doi.org/10.1007/978-94-009-3027-8,
765   1988.

Träumner, K., Kottmeier, C., Corsmeier, U., and Wieser, A.: Convective boundary-layer entrainment: Short review and progress using Doppler lidar, Boundary-layer meteorology, 141, 369–391, 2011.

Träumner, K., Damian, T., Stawiarski, C., and Wieser, A.: Turbulent Structures and Coherence in the Atmospheric Surface Layer, Boundary-Layer Meteorology, 154, 1–25, https://doi.org/10.1007/s10546-014-9967-6, 2015.

770   Virtanen, P., Gommers, R., Oliphant, T. E., Haberland, M., Reddy, T., Cournapeau, D., Burovski, E., Peterson, P., Weckesser, W., Bright, J., van der Walt, S. J., Brett, M., Wilson, J., Millman, K. J., Mayorov, N., Nelson, A. R. J., Jones, E., Kern, R., Larson, E., Carey, C. J., Polat, İ., Feng, Y., Moore, E. W., VanderPlas, J., Laxalde, D., Perktold, J., Cimrman, R., Henriksen, I., Quintero, E. A., Harris, C. R., Archibald, A. M., Ribeiro, A. H., Pedregosa, F., van Mulbregt, P., and SciPy 1.0 Contributors: SciPy 1.0: Fundamental Algorithms for Scientific Computing in Python, Nature Methods, 17, 261–272, https://doi.org/10.1038/s41592-019-0686-2, 2020.

775   Werner, C.: Doppler wind lidar, in: Lidar, pp. 325–354, Springer, 2005.